IMPROVED CHARGE TRANSFER AND BARRIER LOWERING ACROSS A Au-MoS_2 INTERFACE THROUGH THE INSERTION OF A LAYERED Ca_2N ELECTRIDE

by

Fouad Kaadou

Submitted in partial fulfillment of the requirements
for the degree of Master of Science

at

Dalhousie University
Halifax, Nova Scotia
August 2021

This thesis is dedicated to A. A.

Contents

List of Tables

List of Figures

Abstract

Transition-metal dichalcogenides (TMDCs) are a family of layered semiconductors with great potential to impact the upcoming field of two-dimensional (2D) electronics. In particular, MoS_2 is a TMDC with a desirable band gap for the construction of transistors, solar cells, and biochemical sensors. Despite immense promise, use of TMDCs in electronics applications is hindered by the difficulties in forming effective metal contacts with low resistance, as required in any practical device. Although to varying degrees, transition metals spanning the entire *d*-block of the periodic table fail to form proper ohmic contact with MoS_2.

In this work, we propose insertion of a two-dimensional electride $[Ca_2N]^+(e^-)$, an electron rich material, at a metal–TMDC interface to establish proper electrical contact. As a proof-of-concept, we study a Au–Ca_2N–MoS_2 heterostructure and compare it to a Au–MoS_2 heterostructure within a density-functional theory framework using the exchange-hole dipole moment dispersion model. We choose Au since it is a common metal and its interface with MoS_2 leads to a van der Waals gap that is known to exhibit strong Fermi-level pinning, as well as forming high Schottky and tunneling barriers.

Calculations predict nearly complete charge transfer from the electride surface states, resulting in a cationic $[Ca_2N]^+$ monolayer at the interface and metalization of the negatively doped MoS_2. Thus, formation of the Au–Ca_2N–MoS_2 heterostructure eliminates both the tunneling and Schottky barriers, indicating that inserting a single 2D electride layer at metal–TMDC interfaces is a viable strategy to achieve proper ohmic contacts in device manufacture.

Glossary

$C_{n,ij}$	Dispersion coefficients
$E[\rho]$	Total energy functional
$E_{\mathrm{C}}[\rho]$	Correlation energy functional
E_{DFT}	Energy obtained from a self-consistent DFT calculation
$E_{\mathrm{XC}}[\rho]$	Exchange-correlation energy functional
$E_{\mathrm{XC}}^{GGA}[\rho, \nabla\rho]$	GGA exchange-correlation energy
$E_{\mathrm{XC}}^{LDA}[\rho]$	LDA exchange-correlation energy
$E_{\mathrm{X}}[\rho]$	Exchange energy functional
E_{disp}	Dispersion energy correction to E_{DFT}
E_{dist}	Distortion energy
E_{exfol}	Layer exfoliation energy
E_{tot}	Total energy of calculation accounting for both E_{DFT} and E_{disp}
H	Many-body Hamiltonian
N_α	Number of bands
N_k	Number of **k**-points
R_{C}	PP cut-off radius
$R_{c,ij}$	Critical distance between the i^{th} and j^{th} atoms
R_{ij}	Distance between the i^{th} and j^{th} atoms
$T[\rho]$	Kinetic energy functional
T_{KS}	Kohn-Sham kinetic energy
V_{ext}	External potential
Ω	Volume of sample in real space
Ω_j	PP augmented region volume
α	Band index number
α_i	Atomic polarizability
$\langle p_i\vert$	Projector functions
δ_{ij}	Kronecker delta

ϵ_0	Permitivity of free space
$\hat{\mathcal{T}}_j$	Atom-centred PAW operator
$\hat{n}$	Normal vector to density surface
$\hbar$	Reduced Planck constant
$\langle M_l^2 \rangle$	Multipole-moment integrals
$\mathbf{G}$	Reciprocal lattice vector
$\mathbf{I}$	Identity operator
$\mathbf{L}$	Cut-off radius for summation over neighboring cells
$\mathbf{R}$	Lattice translation vector
$\mathbf{a}_i$	Lattice basis vectors
$\mathbf{b}_i$	Reciprocal lattice unit vectors
$\mathbf{k}$	Momentum wavevector
$\mathbf{r}$	Position vector
$\mathcal{F}$	Fourier transform operator
$\mathcal{P}$	Projection operator
$\mathcal{S}$	Spilling parameter
$\mathcal{T}$	PAW operator
$\nabla\rho$	Density gradient
ϕ_i^{KS}	KS basis set
ϕ_i^{PP}	PP basis set
ψ^{PP}	Psuedopotential states
$\psi_i(\mathbf{r})$, ψ^{KS}	Kohn-Sham states
$\psi_k^{\alpha}(r)$	Electron state in a solid with momentum $\mathbf{k}$ occupying band α
$\psi_{s,p,d}$	PP angular momentum orbital states
ρ	Electron density
ε	Energy of Kohn-Sham state
a, c	Cell parameters
a_1, a_2	XDM fitted model parameters
c_i	State coefficients

e	Charge of electron
$e^{i\mathbf{k}\cdot\mathbf{r}}$	Planewave with momentum $\mathbf{k}$
f_n	Becke-Johnson damping function
m	Mass of electron
$u_k^\alpha(r)$	Periodic Bloch function
2D	Two-dimensional
BZ	Brillouin zone
DFT	Density-functional theory
FL	Fermi level
GGA	Generalized gradient approximation
IBZ	Irreducible Brillouin zone
ILDOS	Integrated local density of states
LDA	Local density approximation
NFEG	Near free-electron gas
PAW	Projector-augmented wave method
PBE	Perdew, Burke, and Ernzerhof GGA exchange-correlation functional
PP	Psuedopotential
TMDC	Transition metal dichalcogenide
vdW	van der Waals

XDM Exchange-hole dipole moment dispersion model

Acknowledgements

Much of this thesis was done during the COVID–19 pandemic of 2020–2021. Working in isolation was straining to say the least. I don't believe this project would have come to fruition without the continuous guidance and support of my supervisors Dr. Jesse Maassen and Dr. Erin Johnson. Their technical guidance comes second to the understanding and compassion they have always displayed. I am forever thankful.

Although we did not get to spend a lot of time together this year, I am very grateful to the lads of Dunn 207: Cameron Rudderham, Patrick Strongman, Andrey Zelenskiy, Kelsey Gsell, Dave Kalliecharan and the many other welcomed distractions. I am also forever indebted to Tanya Timmins, our grad coordinator 'mom'.

Of course, thank you to my friends on both sides of the Atlantic Ocean: Peter Makhoul, Lynn Chehin, Mason Maxwell, Erin Lyle, Chris Peacock, Finlay Rankin and Molly Hayes. Last but not least I would like to thank my parents Marwan and Rita; I love you.

Chapter 1

Introduction

The advent of solid-state transistors has launched mankind into the digital age. It is almost impossible to imagine modern life without the seemingly boundless pervasiveness of modern technology. Since its inception almost seven decades ago, the transistor has been continuously shrinking. This perpetual feat of innovation has allowed manufactures to produce more densely packed microchips, allowing our computing power to increase exponentially. Modern transistors are based on traditional silicon-based technology. Despite its tremendous success, this method of assembling transistors is reaching its limits as manufacturers cannot physically make them any smaller. This heralds bad news for a world whose demand for computational power is rampantly growing. Beginning with the discovery of graphene [1], the 21st century has seen the arrival of two-dimensional (2D) materials. These novel materials exhibit exotic electronic properties, such as superconductivity and the quantum hall effect. Of these exciting new 2D materials, transition metal dichalcogenides (TMDCs) have emerged as an extremely promising alternative to silicon for use in future transistor technology [2]. However, TMDC-based technology is not without its own challenges.

Molybdenum disulfide (MoS_2) is a layered TMDC, sometimes referred to as the semiconducting cousin of graphene. In its bulk form, MoS_2 is an indirect-gap semiconductor; however, it transforms into a direct-gap semiconductor when exfoliated to form a single layer [3]. Its bandgap (1.8 eV) [3] makes MoS_2 a strong candidate for use in many electronic and optical applications and devices. It has shown promise in next-generation chemical [4] and biological [5] sensing, transistors [2], and solar cells [6]. Along with other van der Waals (vdW) materials, MoS_2 and graphene are ushering in a new age of 'designer heterostructures' constructed by thoughtfully layering these 2D materials [7].

Unfortunately, the promise of MoS_2 in electronics applications is hampered by the high contact resistance at metal-MoS_2 interfaces, reported to be three orders

of magnitude greater than the predicted minimum contact resistance [8]. Unlike the surface of Si and other bulk semiconductors, layered MoS_2 does not have any dangling bonds in the out-of-plane direction. This makes it challenging for MoS_2 to form proper top contacts with common metals [8, 9, 10, 11, 12]. Instead, many metal-MoS_2 interfaces are held together by weak vdW interactions. This adds an extra potential barrier through which charge carriers must tunnel to cross into the MoS_2 layer. The addition of this tunneling barrier to the already present Schottky barrier at the interface serves to increase the contact resistance [9, 11].

Device performance greatly depends on the particular metal chosen to construct the interface [13, 14]. Although some metals, such as Au, tend to form poor, vdW contacts with MoS_2, experimental and theoretical work has shown that other metals interface more favourably [10, 11, 13]. Despite not having low work functions (as required by the Schottky-Mott rule), Ti and Mo form the best contacts [11, 15, 16] with MoS_2 due to strong orbital overlap with the surface sulfur atoms [11]. Sc has also been shown to interface well with MoS_2 [13], but no known theoretical work has been conducted to explain the underlying mechanism behind this favourable bonding. However, the contacts formed at these metal-MoS_2 interfaces are still not truly ohmic due to the presence of a Schottky barrier and evidence of Fermi-level pinning [11, 13, 15]. The Fermi-level pinning results from a combination of modification of the metal work function due to an interface-induced dipole and the rise of new gap states with Mo *d*-orbital character owing to weakened intralayer Mo–S bonding [17].

To develop an improved contact, Farmanbar et al. suggested placing a single layer of hexagonal boron nitride (h-BN), an insulator, between MoS_2 and cobalt based on density-functional theory (DFT) modelling [18]. The presence of the intermediate h-BN layer destroys the Mo gap states, thus eliminating any Fermi-level pinning and the Schottky barrier at the Co–MoS_2 interface [18]. These DFT predictions were later confirmed experimentally by Cui et al. [19] who successfully engineered a low-resistance Co–h-BN–MoS_2 interface. In this work, we alternatively propose the insertion of a layered electride, Ca_2N, at a metal-MoS_2 interface. We anticipate that the electron-rich nature of the electride will prove beneficial in establishing an ohmic contact and easing charge transport.

Electrides [20] are a class of ionic solids in which the anion is an excess electron, as opposed to a negatively charged ion. The excess electrons, resulting from spontaneous ionization of one or more metal atoms per formula unit, are confined by the surrounding cationic lattice to varying degrees (dimensions). Early syntheses produced organic electrides based on complexes of alkali-metal atoms with electron-rich ligands, such as crown ethers and cryptands, that are characterized by zero-dimensional or one-dimensional electron confinement [21, 22, 23, 24, 25, 26]. However, the majority of the organic electrides are not stable at room temperature [26]. Matsuishi et al. were the first to successfully synthesize a highly stable zero-dimensional inorganic electride, $[Ca_{24}Al_{28}O_{64}]^{4+}(4e^{-})$ [27]. Their success has since encouraged the search for other inorganic electrides that lead to the discovery of one- and two-dimensional electrides [28, 29, 30]. Ca_2N was the first 2D layered electride to be identified [30]. It consists of positively charged $[Ca_2N]^{+}$ layers, with the excess electrons confined between them in 2D interstitial regions.

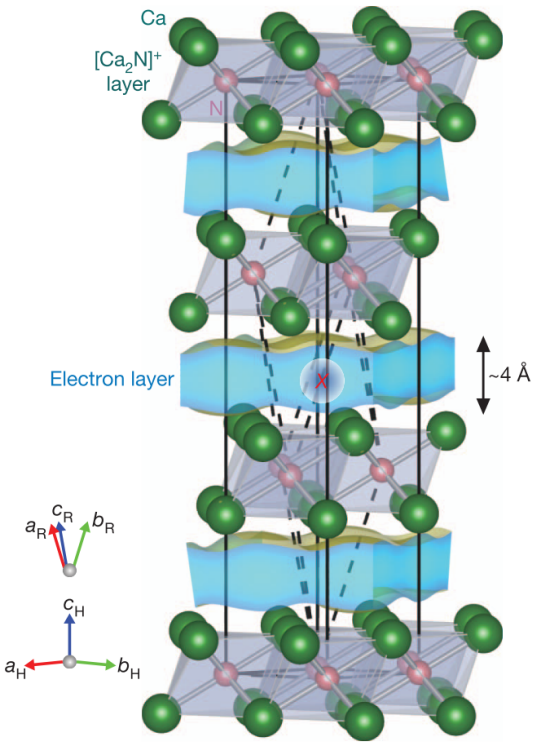

Figure 1.1: Ca_2N structure showing both conventional (solid) and primitive (dashed) cells. Excess electron states (blue) are confined between $[Ca_2N]^{+}$ layers [30]. Included with permission from the publisher (Appendix A).

Ca_2N can be synthesized by a variety of methods [31]. The ionic nature of Ca_2N, with 2D electron localization between the cationic layers, was suggested as early as 1968 when its crystal structure was first determined [32] and early DFT calculations also suggested this unusual electronic structure [33]. However, it was not until recently that, through a combination of computational and experimental work, Lee et al. confirmed its $[Ca_2N]^+(e^-)$ electride stoichiometry [30]. They also demonstrated a high in-plane electron mobility (520 $cm^2V^{-1}s^{-1}$) and carrier concentration ($1.4\times10^{22}cm^{-3}$), long mean free path (0.12 μm), and low anisotropic work function ($\approx$2.6 eV in the (100) plane and $\approx$3.5 eV in the (001) plane).

Ca_2N's favourable transport properties are attributed to the delocalized nature of the electrons confined to the 2D interstitial regions. Angle-resolved photoelectron spectroscopy measurements reveal a cylindrical Fermi surface about the k_z axis in the Brillouin zone, supporting the nearly free nature of the anionic electrons in the xy plane [34], in agreement with previous DFT calculations [30]. The novel properties of Ca_2N have inspired systematic searches for other 2D electrides [35, 36, 37, 38, 39]. Ca_2N has potential applications for use in materials engineering [40, 41], catalysis [42, 43], batteries [44], and electronics [30].

As with other layered materials, there is interest in exfoliating Ca_2N and studying the properties of its monolayer [33, 45, 46, 47]. In the bulk, the excess electrons occupy delocalized interstitial states between the ionic slabs; however, a monolayer sample possesses surface states of similar free-electron character [45, 46, 48]. The differing stabilities of the interstitial versus surface states have the potential to alter the properties of monolayer (or few-layer) Ca_2N relative to the bulk. Zhao et al. performed calculations demonstrating the mechanical and dynamical stability of monolayer Ca_2N and estimated an increased electron mobility due to reduced phonon scattering [45, 49]. Monolayer Ca_2N was since successfully isolated via liquid exfoliation [47]. However, Ca_2N is highly reactive in ambient air, rapidly oxidizing in the presence of O_2 and reacting violently with water to produce ammonia [31]. Encapsulation schemes involving graphene or graphane have thus been proposed to shelter monolayer Ca_2N from its environment [45, 50].

Previous theoretical [51] and experimental [40] studies have investigated the interface between monolayer Ca_2N and $MoTe_2$, a layered TMDC with the same structure as MoS_2. Due to its low work function, Ca_2N readily donates electrons to $MoTe_2$, heavily doping it enough to induce a phase transition from a semiconductor to a metal. This is accompanied by a geometric distortion of the $MoTe_2$ layer, from a hexagonal to a monoclinic structure, with alternating chalcogen atoms displaced towards and away from the Ca atoms of the electride [40, 51]. Of central importance to this work, Dhakal et al. have taken Raman spectroscopy measurements that show significant charge transfer between Ca_2N and bulk MoS_2 [52]. The charge transfer was also accompanied by similar structural changes to the TMDC. These results suggest the promise of introducing a 2D electride at metal-TMDC interfaces to reduce contact resistance and facilitate charge injection into the TMDC.

Here, we use DFT to investigate the bonding of Ca_2N to MoS_2 and gauge the efficacy of its potential use as an interfacial material between MoS_2 and a metal surface to establish an ohmic contact. Examination of the electrostatic potential and charge transfer characteristics across the metal-Ca_2N-TMDC heterostructure shows favourable features for low contact resistance and high electron transport. Chapter 2 outlines the theoretical background behind the calculations used in this work. Chapter 3 contains the preliminary parameter convergence tests. Chapter 4 discusses the Ca_2N-MoS_2 interface and presents a proof-of-concept initial study of the Au-Ca_2N-MoS_2 heterostructure. Finally, Chapter 5 concludes this thesis with an eye for potential future work.

Chapter 2

Theory and Methods

In this chapter, we present a broad overview of the quantum mechanical theories and approximations that underlie the computational methods used to obtain the results of following chapters. This chapter also covers some of the relevant details pertaining to the computational methods used in this work. All density-functional theory calculations were performed with the Quantum ESPRESSO program [53].

2.1 Electronic States in Periodic Solids

The materials studied in this work are examples of crystalline solids. These structures exhibit a discrete periodicity generated by repeating a unit cell over all space. Given the position of the atoms in a unit cell and the lattice vectors $\{\mathbf{a}_i\}$ containing it, every other atomic position can be determined by a translation $\mathbf{R} = n_1\mathbf{a}_1 + n_2\mathbf{a}_2 + n_3\mathbf{a}_3$ where $n_i \in \mathbb{Z}$. A periodic solid is therefore completely specified by its unit cell and a set of translations $\{\mathbf{R}\}$. By enforcing periodic boundary conditions, the periodicity of the system can be exploited to refine the problem of determining the properties of infinitely-sized materials to determining such properties within only a single unit cell.

The many-body Hamiltonian governing the electrons in a unit cell is given by

$$H = \sum_{i}^{N} -\frac{\hbar^2}{2m}\nabla_i^2 + \frac{1}{2}\sum_{i\neq j}^{N} \frac{e^2}{4\pi\epsilon_0\,|\mathbf{r}_i - \mathbf{r}_j|} + V_{\text{ext}}(\mathbf{r}), \tag{2.1}$$

where the first and second terms describe the electron kinetic energy and the electron-electron interaction, respectively. The last term is the external potential, which describes the interaction between the electrons and the ions in the unit cell. Therefore, $V_{\text{ext}}(\mathbf{r}) = V_{\text{ext}}(\mathbf{r} + \mathbf{R})$ contains all the symmetries of the solid and uniquely specifies the solution to Equation 2.1. For the rest of the sections, all quantities will be expressed in atomic units, where $\hbar = m = e = 4\pi\epsilon_0 = 1$.

In 1929, Bloch [54] showed that, in the presence of a periodic external potential, $V_{\text{ext}}(\mathbf{r})$, the eigenfunction solutions to the time-independent Schrodinger equation

must be of the form

$$\psi_k^\alpha(r) = e^{i\mathbf{k}\cdot\mathbf{r}} u_k^\alpha(r), \tag{2.2}$$

where $\mathbf{k}$ is a momentum wavevector eigenvalue and α refers to the band index. An electron's state is therefore the product of a planewave and a function $u_k^\alpha(r)$ that retains the periodicity of the crystal structure. Due to the large number of electrons in a solid, the states are infinitesimally separated in k-space. More specifically, the separation between states in k-space is inversely proportional to the sample volume. Therefore, in the limit of an infinite volume, the energy spectrum – also known as a band structure – is continuous in k but consists of discrete bands.

This result indicates that it may be convenient to describe the unit cell in a Hilbert space spanned by momentum eigenstates of a free electron, i.e. planewaves. The change of basis from position to momentum is achieved by a Fourier transform, $\mathcal{F}$, with the new space known as reciprocal space, or simply k-space. Since the external potential has the periodicity of the lattice, it can be written as a Fourier series over the reciprocal lattice vectors, $\mathbf{G}$,

$$V_{\text{ext}}(\mathbf{r}) = \sum_{\mathbf{G}} V_{\text{ext}}(\mathbf{G}) e^{i\mathbf{G}\cdot\mathbf{r}} \tag{2.3}$$

The reciprocal lattice vectors $\{\mathbf{G}\}$ are expressed in terms of the reciprocal basis vectors $\{\mathbf{b}_i\}$ that are related to the real space basis vectors $\{\mathbf{a}_i\}$ by

$$\mathbf{b}_1 = \frac{2\pi \mathbf{a}_2 \times \mathbf{a}_3}{\mathbf{a}_1 \cdot (\mathbf{a}_2 \times \mathbf{a}_3)}, \qquad \mathbf{b}_2 = \frac{2\pi \mathbf{a}_3 \times \mathbf{a}_1}{\mathbf{a}_1 \cdot (\mathbf{a}_2 \times \mathbf{a}_3)}, \qquad \mathbf{b}_3 = \frac{2\pi \mathbf{a}_1 \times \mathbf{a}_2}{\mathbf{a}_1 \cdot (\mathbf{a}_2 \times \mathbf{a}_3)}. \tag{2.4}$$

The unit cell in reciprocal space is known as the Brillouin Zone (BZ), named after french physicist Léon Brillouin [55]. The calculation of most physical quantities involves the summation over states in the BZ:

$$\sum_k \to \frac{\Omega}{(2\pi)^3} \int d\mathbf{k}. \tag{2.5}$$

In the bulk limit, the sum is converted to an integral, with Ω being the volume of the solid in real space. This is due to the spacing between momentum states, $d\mathbf{k} = (2\pi)^3/\Omega$, becoming infinitesimally small as the volume goes to infinity.

2.2 Density-Functional Theory

2.2.1 Kohn-Sham Theory

Unfortunately, the many-body Schrödinger equation presented in the previous section is hopelessly impossible to solve in its current representation. Even though it need only be solved within a single unit cell, there exists no practically tractable method of solving the interacting-electron eigenvalue problem exactly.

In 1964, Hohenberg and Kohn shed some light on this issue. In their seminal work [56], they introduced two theorems that laid the foundation for the field of density-functional theory (DFT) and its application. The first stated that the external potential, $V_{\text{ext}}(\mathbf{r})$, experienced by a system of electrons, is uniquely determined by the ground state electron density, $\rho_0(\mathbf{r})$. Since the Hamiltonian is uniquely defined by the external potential, this implies that all quantities of the system are also uniquely determined by $\rho_0(\mathbf{r})$. This immense triumph greatly reduces the complexity of solving an N-body Schrödinger equation from 3N-dimensions (where N is on the order of Avogadro's number) to only 3-dimensions. The second Hohenberg-Kohn theorem states that the energy functional, $E[\rho]$, of the system is minimized at the ground state electron density, $\rho_0(r)$. This means that the ground state energy can be obtained via a variational optimization over the electron density.

Although quite powerful, the Hohenberg-Kohn theorems are only existence proofs, i.e. they guarantee the existence of a ground state energy, $E_{\text{GS}}[\rho_0]$, but do not prescribe a method of attaining it. Given the form of the energy functional,

$$E[\rho] = T[\rho] + \frac{1}{2}\int \frac{\rho(\mathbf{r})\rho(\mathbf{r}')}{|\mathbf{r}-\mathbf{r}'|} d\mathbf{r}d\mathbf{r}' + \int \rho(\mathbf{r})V_{\text{ext}}(\mathbf{r})d\mathbf{r} + E_{\text{XC}}[\rho], \tag{2.6}$$

where the terms are the kinetic energy, classical electron-electron interaction, electron-ion interaction, and exchange-correlation energy, respectively, the obstacle of determining the density and exact form of $T[\rho]$ and $E_{\text{XC}}[\rho]$ remains.

Only a year after the publication of the Hohenberg-Kohn theorems, Kohn and Sham presented a recipe for determining $\rho(\mathbf{r})$ [57]. Their formulation, known as Kohn-Sham (KS) theory, is the most common implementation of DFT. KS theory assumes a system of non-interacting electrons with a density

$$\rho(\mathbf{r}) = \sum_{i}^{N} \psi_i^*(\mathbf{r})\psi_i(\mathbf{r}), \tag{2.7}$$

where the single-particle wavefunctions are orthogonal, $\langle\psi_i|\psi_j\rangle = \delta_{ij}$. Within this basis, the total kinetic energy of the particles is

$$T_{\mathrm{KS}} = \sum_{i}^{N} -\frac{1}{2} \langle\psi_i| \nabla^2 |\psi_i\rangle . \tag{2.8}$$

Note that T_{KS} only approximates $T[\rho]$. The discrepancy between T_{KS} and $T[\rho]$ is absorbed into $E_{\mathrm{XC}}[\rho]$ such that

$$E_{\mathrm{XC}}[\rho] = T[\rho] - T_{\mathrm{KS}}[\rho] + E_{\mathrm{X}}[\rho] + E_{\mathrm{C}}[\rho]. \tag{2.9}$$

Using the fact that the total energy, $E[\rho]$, is stationary with respect to $\{\psi_i\}$, the ground state energy may be found by solving the set of equations

$$\frac{\delta E[\rho]}{\delta \psi_i} - \varepsilon_i \psi_i = 0, \tag{2.10}$$

where the second term is a Lagrange multiplier that preserve the states' orthonormality. Taking the appropriate functional derivatives of Equation 2.6 leads to the Kohn-Sham equations,

$$\left(-\frac{1}{2}\nabla^2 + \int \frac{\rho(\mathbf{r})}{|\mathbf{r} - \mathbf{r}'|} d\mathbf{r} + V_{\mathrm{ext}}(\mathbf{r}) + \frac{\delta E_{\mathrm{XC}}[\rho]}{\delta \rho} \right) \psi_i = \varepsilon_i \psi_i. \tag{2.11}$$

These are a set of N single-particle Hamiltonians describing the motion of an independent electron in the presence of some effective potential,

$$V_{\mathrm{eff}}(\mathbf{r}) = \int \frac{\rho(\mathbf{r})}{|\mathbf{r} - \mathbf{r}'|} d\mathbf{r} + V_{\mathrm{ext}}(\mathbf{r}) + \frac{\delta E_{\mathrm{XC}}[\rho]}{\delta \rho}, \tag{2.12}$$

with the last term containing all the many-body quantum-mechanical effects. The KS equations can then be solved self-consistently by picking a starting point for the states $\{\psi_i\}$, obtaining the corresponding electron density, solving the KS equations for an updated set of states $\{\psi_i'\}$, and then computing a new density and comparing with the previous one until convergence of the density and resulting energy is achieved.

If $E_{\mathrm{XC}}[\rho]$ were known, then the KS equations would lead to an exact solution of the Schrödinger equation. However, the exact form of exchange-correlation functional is not known and must be approximated. The two most popular types of exchange-correlation functionals in solid state physics are the local density approximation (LDA) and the generalized gradient approximation (GGA). The LDA approximates

the exchange-correlation energy of the system with that of a uniform electron gas, $E_{\mathrm{XC}}^{LDA}[\rho]$, taking into consideration the local electron density only [57]. Although not a particularly physical representation of chemical systems, it tends to produce accurate results in a range of solids with slowly varying electron densities (i.e. bulk metals). However, this coarse approximation tends to over-bind systems, with its successes often attributed to a cancellation of errors rather than properly incorporated physics. GGAs improve upon this by taking into consideration variations in the electron density with the addition of an electron gradient term, $E_{\mathrm{XC}}^{GGA}[\rho, \nabla\rho]$[58]. All DFT calculations in this work used the GGA exchange-correlation functional of Perdew, Burke, and Ernzerhof (PBE) [59].

2.2.2 The Exchange-Hole Dipole Moment (XDM) Dispersion Model

Dispersion interactions are not currently incorporated in any of the popular base functionals and must be accounted for separately. These interactions contain essential physics required to accurately model layered materials. A dispersion correction is often added to the energy at the end of a self-consistent calculation:

$$E_{\mathrm{tot}} = E_{\mathrm{DFT}} + E_{\mathrm{disp}}. \tag{2.13}$$

In this work, dispersion interactions are treated with the exchange-hole dipole moment (XDM) model [60, 61, 62], which has been shown to be highly accurate for TMDCs and other layered materials [63]. XDM's formulation is based on the instantaneous dipole moment induced between an electron and its exchange-hole counterpart as the source of dispersion interactions. Although not based on a first-principles approach, its derivation is supported by strong physical motivation, as evidenced by its remarkable performance.

In a periodic, solid-state system, the dispersion energy correction is given by

$$E_{\mathrm{disp}} = -\frac{1}{2} \sum_{n=6,8,10} \sum_{\mathbf{L}} \sum_{i \neq j} \frac{C_{n,ij} f_n\left(R_{ij,\mathbf{L}}\right)}{R_{ij,\mathbf{L}}^n}, \tag{2.14}$$

where $\{C_{n,ij}\}$ are the dispersion coefficients, f_n is the Becke-Johnson damping function, and R_{ij} is the interatomic distance between the i^{th} and j^{th} atom. The sum runs over all atoms in the unit cell and includes interactions with neighbouring atoms in adjacent cells within a discrete cut-off radius, and $\mathbf{L}$ is some multiple of lattice unit vectors.

The dispersion coefficients are given by

$$C_{6,ij} = \alpha_i \alpha_j \frac{\langle M_1^2 \rangle_i \langle M_1^2 \rangle_j}{\alpha_j \langle M_1^2 \rangle_i + \alpha_i \langle M_1^2 \rangle_j}, \tag{2.15}$$

$$C_{8,ij} = \frac{3}{2} \alpha_i \alpha_j \frac{\langle M_1^2 \rangle_i \langle M_2^2 \rangle_j + \langle M_2^2 \rangle_i \langle M_1^2 \rangle_j}{\alpha_j \langle M_1^2 \rangle_i + \alpha_i \langle M_1^2 \rangle_j}, \tag{2.16}$$

$$C_{10,ij} = \alpha_i \alpha_j \frac{2\langle M_1^2 \rangle_i \langle M_3^2 \rangle_j + 2\langle M_3^2 \rangle_i \langle M_1^2 \rangle_j + \frac{21}{5} \langle M_2^2 \rangle_i \langle M_2^2 \rangle_j}{\alpha_j \langle M_1^2 \rangle_i + \alpha_i \langle M_1^2 \rangle_j}, \tag{2.17}$$

where the multipole-moment integrals, $\langle M_l^2 \rangle$, are calculated from the electron density and the atomic polarizabilities, α_i, are environment dependent. This is why XDM is known as a minimally-empirical dispersion model. Almost all quantities are dependent on the local electron density, i.e. they are non-generic and system dependent. This flexibility lends itself well to a wide variety of systems.

The only fitted model parameters are (a_1, a_2) in the damping function,

$$f_n\left(R_{ij}\right) = \frac{R_{ij}^n}{R_{ij}^n + \left(a_1 R_{c,ij} + a_2\right)^2}, \tag{2.18}$$

where $R_{c,ij}$ is the critical distance between two atoms i and j, and is defined to be the distance at which the set of dispersion terms, $\left\{C_{n,ij}/R_{ij}^n\right\}$, become equal. The fitting parameters (a_1, a_2) are dependent on the functional and must be defined at the beginning of a DFT calculation.

2.3 Pseudopotentials and the Projector Augmented-Wave Method

As discussed previously, planewaves are a well-suited basis to describe electrons in periodic solids. However, near the core, valence states tend to oscillate rapidly as a consequence of requiring orthogonality with the core states. An accurate description of these states would require a large set of planewaves. Fortunately, core electrons do not directly contribute to the interactions between atoms in molecules or solids. Their main effect is to screen the Coulombic potential of the nucleus, i.e. they can be effectively removed from the Hamiltonian without altering the chemistry of the system. This reduces the eigenvalue problem to only solving for valence states, where the effect of the core electrons can be incorporated through the use of a

pseudopotential (PP) [64] that replaces V_{ext}. Modifying the Hamiltonian in such a way results in a transformation of the original KS eigenvalue problem. The new valence eigenstates, $\{\psi_i^{\text{PP}}\}$, are not the same as the original KS states, $\{\psi_i^{\text{KS}}\}$. However, the pseudopotential is constructed such that the valence electron states are the same past some cut-off distance, R_{C}, away from the nucleus, conserving the chemical properties of the atom.

One approach to PP calculations is the projector augmented-wave (PAW) method [65], which segments the wavefunction into two pieces. The outer segment, $r > R_{\text{C}}$, is described by planewaves, while the inner augmented segment, $r < R_{\text{C}}$, is constructed from smooth partial waves. The central advantage of the PAW method is that it is not strictly an approximation. Instead, it is a reformulation of the KS problem via a linear transformation, $\mathcal{T}$, that preserves the information in the original KS states $\{\psi_i^{\text{KS}}\}$. The KS states are then related to the pseudo-wavefunction by

$$|\psi^{\text{KS}}\rangle = \mathcal{T}\,|\psi^{\text{PP}}\rangle\,. \tag{2.19}$$

Since ψ^{PP} must match ψ^{KS} outside the augmented region, the transformation operator can be written as

$$\mathcal{T} = \mathbf{I} + \sum_j \hat{\mathcal{T}}_j, \tag{2.20}$$

where $\mathbf{I}$ is the identity operator and $\hat{\mathcal{T}}_j$ is a an atom-centred operator that is only non-zero within a spherical volume, Ω_j, of radius $R_{\text{C},j}$ surrounding the j^{th} nucleus. Within the augmented region, the pseudo-wavefunctions are constructed from a complete set of partial waves, such as Bessel functions, $\psi^{\text{PP}}(r < R_{\text{C}}) = \sum c_i\,|\phi_i^{\text{PP}}\rangle$. This basis of partial waves is then related to the basis used to describe the core section (within Ω_j) of the KS states via the same transformation, $|\phi^{\text{KS}}\rangle = \mathcal{T}\,|\phi^{\text{PP}}\rangle$.

The states ϕ^{KS} are usually defined to be the solutions to the radial KS Hamiltonian for the case of an isolated atom. Thus, within Ω_j,

$$|\psi^{\text{KS}}\rangle = \mathcal{T}\,|\psi^{\text{PP}}\rangle = \mathcal{T}\sum_i c_i\,|\phi_i^{\text{PP}}\rangle = \sum_i c_i\,|\phi_i^{\text{KS}}\rangle\,, \tag{2.21}$$

and so $|\psi^{\text{KS}}\rangle$ may be written as

$$|\psi^{\text{KS}}\rangle = |\psi^{\text{PP}}\rangle - \sum_i c_i\,|\phi_i^{\text{PP}}\rangle + \sum_i c_i\,|\phi_i^{\text{KS}}\rangle\,. \tag{2.22}$$

The coefficients, c_i, are the same in both sums and are given by $\langle p_i|\psi^{\mathrm{PP}}\rangle$, where $\langle p_i|$ are known as projector functions. The projector functions are orthogonal to $|\phi^{\mathrm{PP}}\rangle$, $\langle p_i|\phi_j^{\mathrm{PP}}\rangle = \delta_{ij}$, and can, in general, be constructed from an arbitrary set of linearly independent functions. The linear operator mapping between $|\psi^{\mathrm{KS}}\rangle$ and $|\psi^{\mathrm{PP}}\rangle$ can thus be expressed as

$$\mathcal{T} = \mathbf{I} + \sum_{i,j} \left(|\phi_{ij}^{\mathrm{KS}}\rangle - |\phi_{ij}^{\mathrm{PP}}\rangle \right) \langle p_{ij}| \,, \tag{2.23}$$

where the sum runs over all orbitals of all atoms in the units cells.

The PAW method is computationally efficient and has the added advantage of retaining the core wavefunctions, which is an important feature for computing properties that depend on the core electrons. The PAW method used in this work is based on the Kresse-Joubert implementation [66].

The above formalism assumes that the augmentation spheres, Ω_j, do not overlap. However, this assumption must be enforced during calculations and failing to do so leads inaccurate energies due to unwanted spurious interactions between the core densities in the overlapped spheres [67]. All PPs used in this work were taken from the Quantum ESPRESSO library [68]. Table 2.1 shows the cut-off radii of all the PPs used. No bonds in any of the systems considered were shorter than the sum of any cut-off radii of the corresponding atoms.

Table 2.1: Pseudopotentials and cut-off radii, R_{C} in Å, for s, p and d orbitals.

Element	Pseudopotential File	ψ_s	ψ_p	ψ_d
Ca	Ca.pbe-spn-kjpaw_psl.1.0.0.UPF	0.64	0.74	n/a
N	N.pbe-n-kjpaw_psl.1.0.0.UPF	0.53	0.48	n/a
Mo	Mo.pbe-spn-kjpaw_psl.1.0.0.UPF	0.58	0.53	0.69
S	S.pbe-n-kjpaw_psl.1.0.0.UPF	0.79	0.79	n/a
Au	Au.pbe-n-kjpaw_psl.1.0.0.UPF	1.06	1.22	0.53

2.4 K-point Sampling and Smearing

Since most physical quantities require integrating over all electron states in the BZ, it is crucial to perform accurate and well-converged integrations over **k**-space. The reliability of our numerical calculations is highly dependent on the coarseness of **k**-space discretization. Given any conventional unit cell, its corresponding BZ inherently possesses redundancies that can be eliminated through the exploitation of the cell's symmetries. Taking advantage of this reduces the volume in **k**-space over which one must integrate, and thus reduces the computational time. The abridged section of the BZ is known as the irreducible Brillouin zone (IBZ), over which all integrations can be evaluated without loss of information. In this work we use the commonly implemented Monkhorst-Pack discretization scheme [69], as it provides a sufficient and efficient **k**-point sampling of the IBZ.

When dealing with metals, one must take care when performing integrations over the occupied **k**-space as discontinuities arise from partially filled bands. Since DFT calculations are performed at absolute zero, the Fermi level (FL) dictates a hard cut-off for state occupations. This is not a problem for the case of semiconductors and insulators, as all their bands are occupied below the FL. However, the sharp discontinuities that originate from metal bands crossing the FL can cause problems with numerical convergence. In order to resolve this, the discontinuities are often replaced by functions that decay to zero smoothly. In this work, we use a Gaussian smearing that replaces the discontinuity with a Gaussian function of a user-defined width, given in units of energy.

2.5 State Projection

When bringing two materials together, strong interactions can drastically affect the electronic band structure. States can disappear or undergo significant change, with the possibility of being replaced by new states. Although states near the FL are the most vulnerable, states further away in energy can also be modified due to structural changes undergone by the host material during the formation of an interface. Simply plotting the band structure of a heterostructure can give some insight to these changes, but often excludes much of the finer detail. More specific features can

be extracted by studying how states are shared between two materials. This requires an appropriate state partitioning scheme. Unfortunately, the delocalized nature of the planewave basis does not lend itself well to the problem. In order to circumvent this issue, we project the individual states, $|\psi_\alpha(\mathbf{k})\rangle$, onto the set of localized atomic orbital wavefunctions taken from the PP file using the projwfc.x code implemented in Quantum ESPRESSO. This projection allows for the convenient separation of each state, $|\psi_\alpha(\mathbf{k})\rangle$, with momentum $\mathbf{k}$ in band α, into individual atomic and orbital components. The contributions can then be simply read out and calculated by summing the coefficients of the wavefunction in the projected basis. The results of such projections are sensitive to the choice of initial and final bases and must not be used to infer quantitative conclusions. However, they still offer important qualitative insight into the evolution of electronic states due to the formation of an interface.

In this work, the method of Sanchez-Portal [70] was used to evaluate the quality of the projection. Given the planewave eigenstates of the KS Hamiltonian, the amount of "spilled" information that is lost when projecting onto the space of localized orbitals can be measured through the spilling parameter, $\mathcal{S}$, which is a number between 0 and 1, with $\mathcal{S} = 0$ indicating a perfect lossless projection. Table 2.2 shows the spilling parameters for the state projections in all heterostructure systems. All spilling parameters are close to 0 and indicate that the projections well represent the initial planewave states. $\mathcal{S}$ is largest for systems containing Ca_2N with a side adjacent to a vacuum. This is to be expected since the un-interfaced portion of Ca_2N contains nearly free-electron states that are difficult to characterize in terms of a localized basis set.

Table 2.2: Spilling parameter for state projections in heterostructures. See chapter 4 for calculation details.

Heterostructure	$\mathcal{S}$ ($\times 10^{-2}$)
Monlayer Ca_2N–MoS_2	1.4
Bilayer Ca_2N–MoS_2	1.3
Trilayer Ca_2N–MoS_2	1.4
Quadlayer Ca_2N–MoS_2	1.5
Au–MoS_2	0.5
Au–Ca_2N–MoS_2	0.7

2.6 Bader Charge Transfer

An essential part of the work presented here focuses on determining the transfer of charge from one material to another. This requires a reliable method of assigning charge to individual nuclei and computing any changes that arise after the formation of an interface. Ascribing peripheral charges within a molecule or solid to a particular atom is a non-trivial matter, as there is no fundamental rule to follow. However, several methods have been proposed to tackle this issue [71, 72, 73].

Here we use the method developed by Bader in his quantum theory of atoms in molecules [71]. Bader's argument is topological and relies upon the gradient of the charge density, $\nabla\rho(\mathbf{r})$, to define atomic structure. For any molecular or solid-state system, the charge density exhibits local maxima at the positions of the nuclei. In other words, the gradient field vanishes at these critical points, $\nabla\rho\left(\mathbf{R}_j\right) = 0$, and is concave about these points, $\nabla^2\rho(\mathbf{r}) < 0$. This convenient fact allows one to define a unique path along $\nabla\rho(\mathbf{r})$ from any point $\mathbf{r}_i$ that terminates at a single nuclear position, $\mathbf{R}_j$, allowing the association of the charge density, $\rho(\mathbf{r}_i)$, with a particular nucleus. This method leads to the partitioning of charges into non-intersecting basins, centred at atomic nuclei, that are separated by a surface of zero flux,

$$\nabla\rho \cdot \hat{n} = 0, \tag{2.24}$$

where $\hat{n}$ is the normal to the surface of the basin.

In practice, $\rho(\mathbf{r})$ is discretized on a spatial grid over which all numerical integrations are performed. For this, we use the algorithm developed by Yu and Trinkle [74]. Their method has been shown to be extremely efficient and accurate when partitioning Bader charges into basins. The main feature of this approach deals with the partitioning that occurs at the zero-flux boundaries on the finite grid. The Yu-Trinkle algorithm allows for the assignment of fractional weights to each descretized volume of charge density. Near a nucleus, this approach is not unique as the weight is unity for that basin; however, allowing fractional assignment at the boundary of different basins turns out to be extremely beneficial. Other algorithms that use binary assignment require finer spatial grids and are thus more expensive. The Yu-Trinkle algorithm not only allows for coarser grids and less computational time, but also out-performs these binary weight algorithms with the same number of grid points.

Finally, the quantity of charge transfer may be defined at each atomic site as the difference in Bader charge when the materials are interfaced together versus when they are separated.

Chapter 3

Preliminary Testing & Calculations

This chapter describes basic preliminary tests conducted to determine the parameters used in the proceeding calculations to guarantee well-converged numeric results. Additionally, due to the choice of dispersion model, optimized lattice parameters had to be determined by manually identifying the minima of potential energy curves. Results are shown for Ca_2N, MoS_2, and Au.

3.1 Parameter Convergence Testing

3.1.1 Planewave Energy Cutoff for the Wavefunction

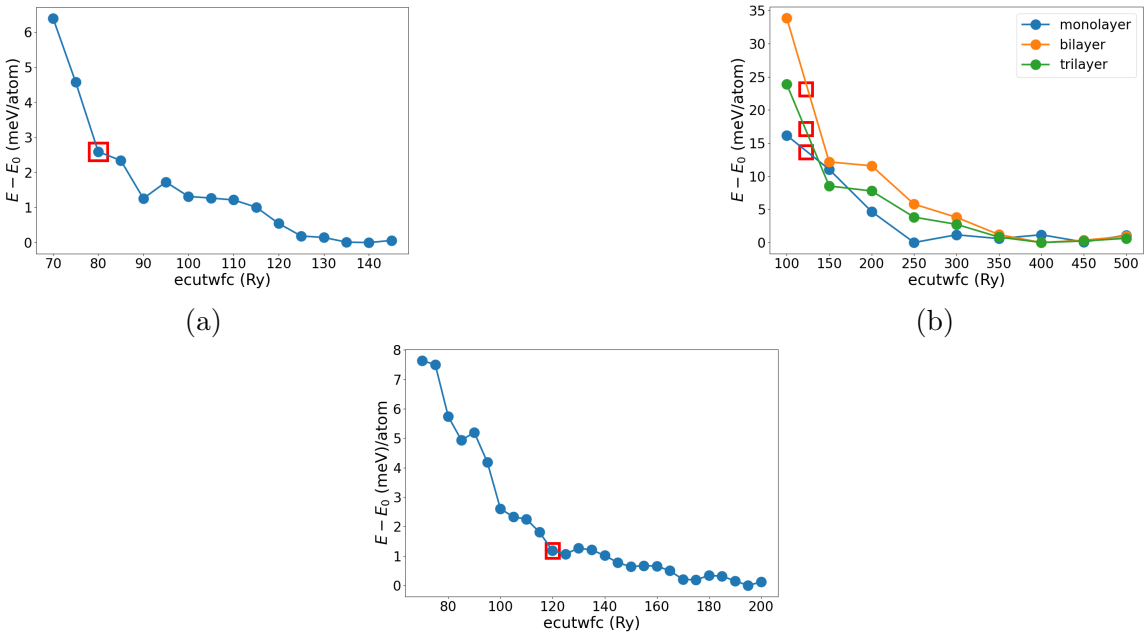

(a) (b)

(c)

Figure 3.1: Convergence tests for the ecutwfc parameter for a) bulk Ca_2N (hexagonal cell), b) layered Ca_2N, and c) monolayer MoS_2 structures, relative to the minimum-energy point on each graph. The red boxes indicate the chosen values – 80 Ry for bulk Ca_2N and 120 Ry for the layered materials.

The first parameter to be converged was the ecutwfc, which determines the size of the planewave basis set for the wavefunction. Fig. 3.1 shows an ecutwfc convergence test performed for bulk Ca_2N, layered Ca_2N, and monolayer MoS_2. A convergence threshold of a few meV per atom was sought. As shown, layered materials require a larger ecutwfc due to the presence of a vacuum layer, which requires that the electronic density quickly decay to zero away from the atomic layer. With the intention of eventually joining the two materials in a single cell to form a heterostructure, the same ecutwfc of 120 Ry was chosen for both Ca_2N and MoS_2. Although an ecutwfc of 120 Ry is not as numerically converged in the case of layered Ca_2N as in monolayer MoS_2, our tests indicate that this choice does not significantly impact the results. Fig. 3.2 shows an overlay of two band structures for monolayer Ca_2N calculated with an ecutwfc of 120 Ry or 250 Ry. The overlay clearly indicates virtually no difference between the large and small ecutwfc values. An ecutwfc of 120 Ry was thus chosen to keep future calculations involving larger heterostructure cells computationally tractable. Further literature review revealed that our choice for ecutwfc exceeds twice the commonly used values in similar calculations for both bulk and layered Ca_2N [30, 33, 45, 46, 75, 76].

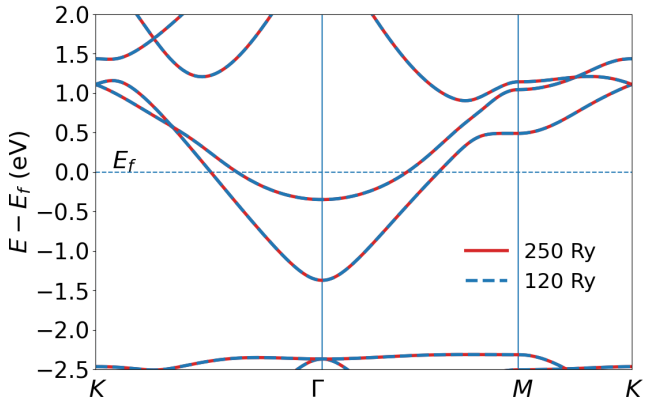

Figure 3.2: Comparison of monolayer Ca_2N band structure with an ecutwfc of 120 Ry or 250 Ry.

3.1.2 Planewave Energy Cutoff for the Electron Density

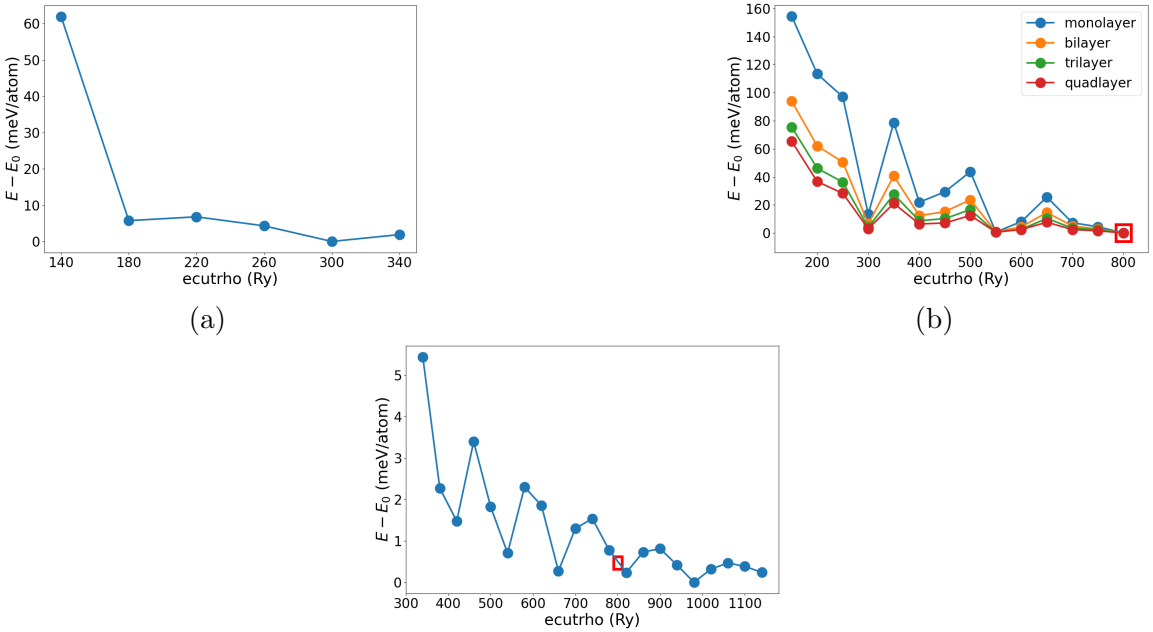

Figure 3.3: Convergence tests for the ecutrho parameter a) bulk Ca_2N (hexagonal cell), b) layered Ca_2N, and c) monolayer MoS_2 structures, relative to the minimum-energy point on each graph. The red boxes indicate the chosen value (800 Ry).

After determining the converged value for ecutwfc, the ecutrho parameter was converged. It determines the coarseness of the real-space grid used in evaluation of the electron density and density-dependent integrals. Fig. 3.3 shows the results of ecutrho convergence tests for bulk Ca_2N, layered Ca_2N, and monolayer MoS_2. A value of 800 Ry for ecutrho was found to be well-converged for the cases of few-layered Ca_2N. This value was also found to be appropriate for monolayer MoS_2 and was thus adopted for both since future calculations would be performed on a heterostructure of the two materials. This value was used in all calculations, including for bulk Ca_2N.

3.1.3 k-grid

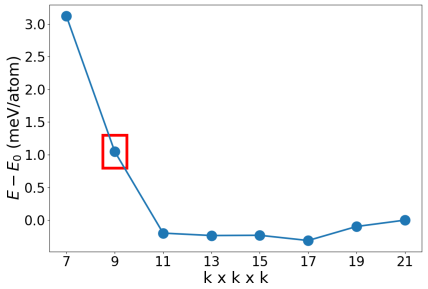

(a)

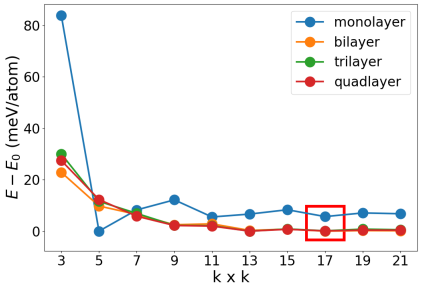

(b)

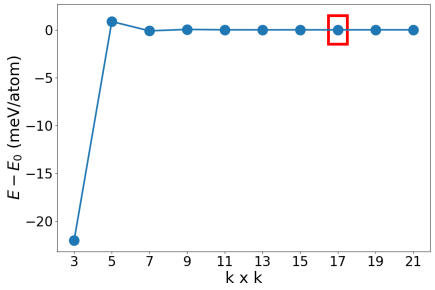

(c)

Figure 3.4: Convergence tests for the in-plane **k**-grid of a) bulk Ca_2N (hexagonal cell), b) layered Ca_2N, and c) monolayer MoS_2 structures, relative to the minimum-energy points on each graph. The red boxes indicate the chosen values.

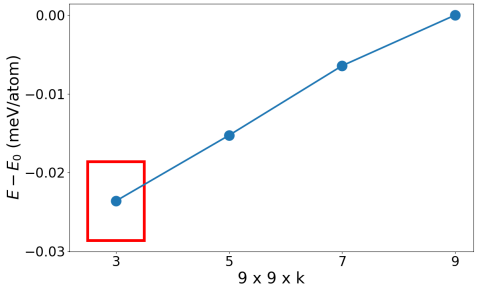

(a)

Figure 3.5: Convergence tests for the out-of-plane **k**-grid of bulk Ca_2N (hexagonal cell), relative to the minimum-energy points on the graph. The red box indicates the chosen value.

Due to the difference in length of the in-plane and out-of-plane lattice vectors of the bulk Ca_2N cell, separate in-plane and out-of-plane values for the **k**-grid must be determined. The out-of-plane **k** value is less than that of the in-plane. Calculations involving layered materials do not require separate convergence of **k** in the out-of-plane direction, since the large vacuum layer aims to break any cross-cell interactions in along z-direction. The above tests were conducted using primitive unit cells for the layered materials. When running calculations for larger cells, the **k** values were reduced proportionally. For example, doubling the cell size would require half the number of **k** points in order to maintain the same spacing, $d\mathbf{k}$, in all cases.

3.1.4 Vacuum layer

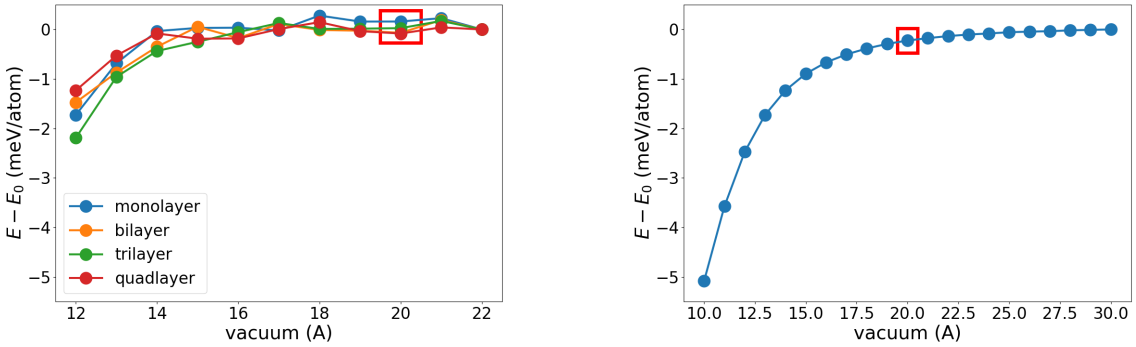

(a) (b)

Figure 3.6: Convergence tests for the vacuum layer atop the a) layered Ca_2N and b) monolayer MoS_2 structures, relative to energy at the largest interlayer distance. The red boxes indicate the chosen value ($\approx$ 20 Å).

Due to periodic boundary conditions, calculations involving layered materials must be padded with a large vacuum layer to minimize any interactions between neighbouring cells in the out-of-plane direction. Convergence tests indicate that a vacuum layer of $\approx$ 20 Å is sufficient.

3.2 Determining Lattice Parameters

The XDM implementation in Quantum ESPRESSO assumes that the dispersion coefficients are static with respect to the charge density (i.e. their derivatives with respect to the charge density is zero) when evaluating the atomic forces and stresses. This means that the forces and stresses are inconsistent with the energy expression at each step of a geometry optimization and performing a relaxation with a variable cell size does not actually yield the optimal cell parameters for the system. While the errors in optimum lattice parameters are negligible for molecular crystals, they can be quite significant for inorganic materials [77]. One must therefore vary the lattice parameters by hand and construct a potential energy curve to determine the true minimum (see table 4.1 for results). Despite this practical difficulty, the cell parameters determined with XDM remain accurate and reliable. However, accurate evaluation of the XDM forces and stresses remains an outstanding challenge.

3.2.1 Bulk Ca_2N

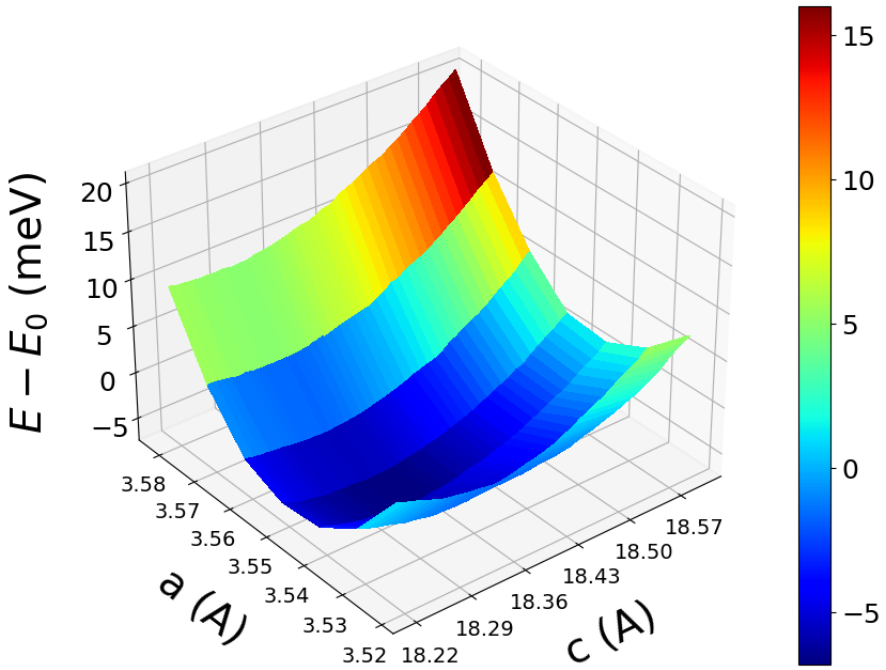

Figure 3.7: Energy of bulk Ca_2N as a function of lattice parameters, relative to its equilibrium geometry.

Plotting the energy of bulk Ca_2N as a function of its in-plane and out-of-plane parameters reveals a minimum at $a = 3.55$ Å and $c = 18.33$ Å, which are in reasonable agreement with experimental values, $a = 3.63$ Å and $c = 18.97$ Å [30], given that the calculations do not take into account contributions from thermal expansion.

3.2.2 Layered Ca_2N

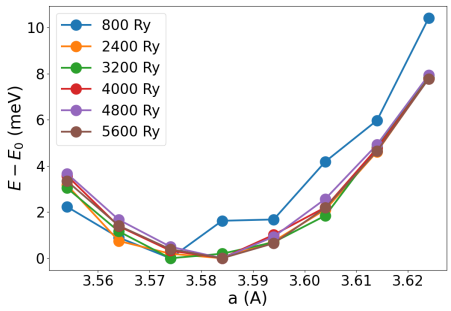

(a) Monolayer Ca_2N

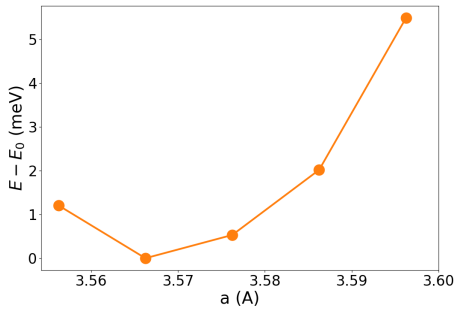

(b) Bilayer Ca_2N

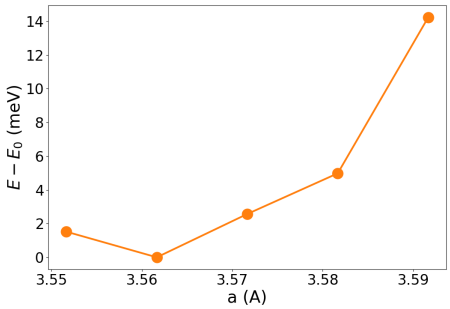

(c) Trilayer Ca_2N

Figure 3.8: Energy as a function of lattice parameters for 1-3 layered Ca_2N, relative to the respective equilibrium geometries. Calculations for monolayer Ca_2N were performed for a range of ecutrho values.

Fig. 3.8a shows the energy of monolayer Ca_2N as a function of its lattice parameter for various values of ecutrho. A value of 800 Ry for ecutrho leads to a rough curve, which prompted the recalculation of the energy using higher ecutrho values. To guarantee smoothness, an ecutrho of 2400 Ry was used to construct the potential energy curves for 2 and 3-layered Ca_2N. Although, an ecutrho of 800 Ry leads to a rough energy curve, the energy fluctuations are insignificant. Therefore, to save on computational time, an ecutrho of 800 Ry was maintained for all other calculations in this work that do not involve finding the optimal lattice parameter of a structure.

The optimized lattice parameters were found to be $a_{\text{mono}} = 3.57$Å, $a_{\text{bi}} = 3.57$Å, $a_{\text{tri}} = 3.56$Å, for the mono-, bi-, and trilayer respectively. All determined lattice parameters are in excellent agreement with previous studies [45, 46, 76]. The bulk lattice parameter, $a_{\text{bulk}} = 3.55$Å, was used for quadlayer Ca_2N, in agreement with previous studies [46]. The Ca_2N lattice parameter tends to decrease with the addition of more layers due to increased in-plane interactions.

3.2.3 Au

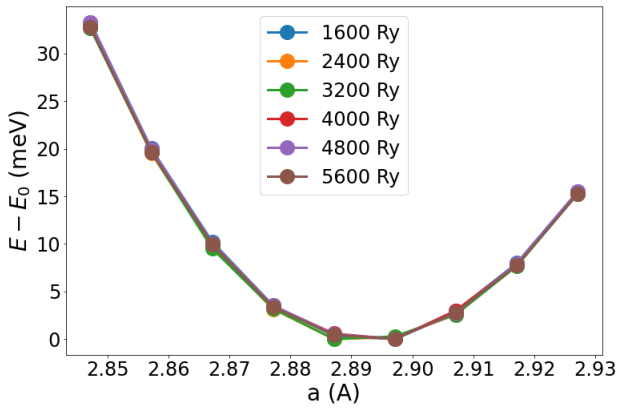

Figure 3.9: Energy of 4-layer Au as a function of the lattice parameter, relative to its equilibrium geometry. Calculations were performed for a range of ecutrho parameters.

From Fig. 3.9, we determine a lattice constant of $a_{\text{Au}} = 2.90$ Å for the (111) face of the primitive 4-layer Au cell. This is in excellent agreement with the known lattice parameter for bulk Au [78], indicating convergence to bulk behaviour. A range of ecutrho values above 800 Ry was used to guarantee smoothness of the curve. However, for the same reasons mentioned in the above section concering the lattice parameters of layered Ca_2N, further calculations used a value of 800 Ry.

Chapter 4

Improved Charge Transport across a Au-MoS_2 Interface through the Insertion of a Layered Ca_2N Electride

This chapter is reproduced from F. Kaadou, J. Maassen and E. R. Johnson, "Improved Charge Transfer and Barrier Lowering across a Au–MoS_2 Interface through Insertion of a Layered Ca_2N Electride". *The Journal of Physical Chemistry C* **2021** *120* (21), 11656-11664. DOI: https://pubs.acs.org/doi/10.1021/acs.jpcc.1c02142/.

4.1 Motivation

Unlike contacts with bulk semiconductors, metals tend to form very poor interfaces with MoS_2 due to the absence of dangling bonds in layered materials. Although to varying degrees, transition metals spanning the entire *d*-block of the periodic table fail to form proper ohmic contacts with MoS_2. This unfortunate obstacle has held back layered semiconductors from breaking into the mainstream and shifting the current technological landscape. However, the quality of a metal–MoS_2 contact may be improved by introducing a layer of Ca_2N, a novel 2D electride, at the interface. As a proof-of-concept, we start by studying the Au–Ca_2N–MoS_2 interface. Of the many choices for a metal, we select Au given that it is the most common contact metal, its interface with MoS_2 is well characterized, and it leads to high tunnelling and Schottky barriers [10, 11]. The electrical properties of the Au–Ca_2N–MoS_2 interface are studied by calculating the electrostatic potential across the heterostructure and the charge transfer resulting from its formation. These quantities help predict the quality of the electrical contact. The results are then compared to the case of a Au–MoS_2 interface.

4.2 Computational Methods

Initial structures used for geometry optimizations of Ca_2N and monolayer MoS_2 were obtained from Refs. [79] and [78], respectively. For bulk Ca_2N using a hexagonal unit cell, the optimized lattice parameters were $a = 3.55$ Å and $c = 18.33$ Å, which are in reasonable agreement with experiment ($a = 3.63$ Å and $c = 18.97$ Å) [30], considering that we are neglecting thermal expansion. Multi-layered Ca_2N slabs were constructed by isolating layers from the bulk Ca_2N cell; their relaxed in-plane lattice constants are shown in Table 4.1. Weaker in-plane interactions lead to slightly greater cell sizes for monolayer and bilayer Ca_2N.

Table 4.1: Optimized in-plane lattice constants, a in Å, for various layered materials and heterojunctions using hexagonal unit cells. For the interfaces, the structures were constructed to avoid strain of the MoS_2 geometry, so the lattice constants are multiples of those used for the MoS_2 monolayer.

Material	Form	a	Number of atoms per unit cell
Ca_2N	Monolayer	3.57	3
Ca_2N	Bilayer	3.57	6
Ca_2N	3-layer	3.56	9
Ca_2N	4-layer	3.55	12
MoS_2	Monolayer	3.18	3
Au	Slab	2.90	4
Ca_2N–MoS_2	Interface	6.36	21
Au–MoS_2	Interface	5.50	25
Au–Ca_2N–MoS_2	Interface	11.00	159

All interfaced structures adopted the MoS_2 cell size, allowing only the atomic positions to vary. The Ca_2N–MoS_2 interfaces were constructed by joining a (2×2) monolayer MoS_2 supercell (Fig. 4.1a) with a $(\sqrt{3} \times \sqrt{3})$ Ca_2N supercell (Fig. 4.1b), resulting in 2.9-3.4% lattice distortion for the Ca_2N layers, depending on thickness. The Au–MoS_2 interface was constructed by joining a $(\sqrt{3} \times \sqrt{3})$ monolayer MoS_2 supercell (Fig. 4.1a) with a 4-layer (2×2) Au supercell (Fig. 4.1c), resulting in a 5.0% lattice distortion for Au. While this amount of lattice strain is fairly high, it can be fairly easily accommodated by soft metals, such as Au, and the corresponding energy penalty is only 88 meV/Å^2 per Au layer. The final Au–Ca_2N–MoS_2 structure was constructed by joining a 6-layer (4×4) Au supercell to a $(\sqrt{3} \times \sqrt{3})$ supercell of the previously constructed monolayer Ca_2N–MoS_2 interface. In order to guarantee a

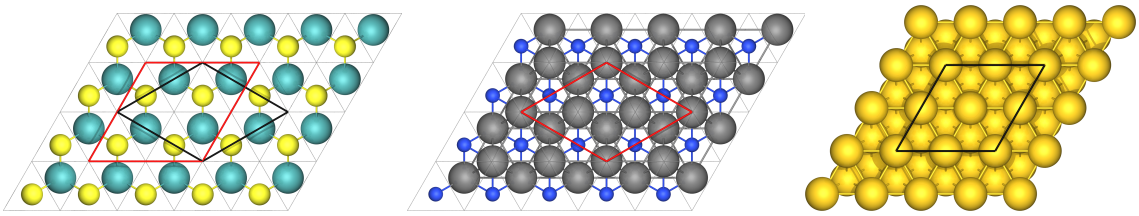

(a) $\sqrt{3} \times \sqrt{3}$ (black) and 2×2 (red) MoS_2 cells

(b) $\sqrt{3} \times \sqrt{3}$ Ca_2N cell

(c) 2×2 Au cell

Figure 4.1: Geometries of the monolayers and surface slab model used to construct each interface. Yellow: S; cyan: Mo; grey: Ca; blue: N; gold: Au.

bulk-like environment away from the interface, the positions of the bottom two layers of Au atoms were held fixed in the z-direction. A vacuum spacing of $\sim$ 20 Å was maintained across all systems to minimize unwanted cross-cell interactions.

All DFT calculations were performed with the Quantum ESPRESSO [53] program, using the Perdew-Burke-Ernzerhof (PBE) [59] exchange-correlation functional, the projector augmented wave (PAW) method [65], and periodic boundary conditions. Dispersion interactions were treated with the exchange-hole dipole moment (XDM) model [60, 61, 62], which has been shown to be highly accurate for TMDCs and other layered materials [63].

Calculations for bulk Ca_2N used planewave cut-off energies of 80 and 800 Ry for the wavefunction and electron density, respectively, and a $9 \times 9 \times 3$ **k**-point grid. Ca_2N–MoS_2, Au–MoS_2, all few-layer Ca_2N structures, MoS_2, and the Au slabs used planewave cut-off energies of 120 and 800 Ry and a $7 \times 7 \times 1$ **k**-point grid. Finally, the Au–Ca_2N–MoS_2 heterostructure used planewave cut-off energies of 120 and 800 Ry. Due to its large unit-cell size, a $2 \times 2 \times 1$ **k**-point grid was used for geometry relaxation, while a subsequent calculation with a $3 \times 3 \times 1$ grid was used to generate the band structure, electrostatic potential, and charge data. All calculations used a Gaussian smearing parameter of 1×10^{-3} Ry. Relaxations of atomic positions used a force convergence threshold of 1×10^{-4} Ry/Bohr. Bader [80] charge integration was conducted using the Yu-Trinkle algorithm [74], as implemented in the critic2 code [81].

4.3 Results and Discussion

4.3.1 Bulk Versus Few-Layer Ca_2N

Before considering heterostructures involving Ca_2N, we first examine the dependence of its electronic structure on the number of 2D layers. Fig. 4.2 shows the band structures of bulk, bilayer, and monolayer Ca_2N, as well as heat maps of the integrated local density of states (ILDOS) near the FL. For bulk Ca_2N, the ILDOS plot shows the anionic electrons (purple) residing in the interstitial gap between the cationic atomic layers. In the band structure, these interstitial states are easily identified as the three bands crossing the FL. The quasi-parabolic shape of these bands and their close resemblance in the K $\rightarrow$ Γ and Γ $\rightarrow$ M segments show the near free-electron gas (NFEG) nature of the anionic electrons along the in-plane direction. Although bulk Ca_2N is a metal at standard temperature and pressure, as indicated by the band structure, it is possible to induce a metal-to-semiconductor transition at higher pressures [82] or via semi-hydrogenation [83].

Exfoliated layers of Ca_2N retain the same stoichiometry as the bulk [47]. In fact, the band structure of the bilayer is largely unchanged with respect to the bulk, with the major exception that the interstitial states at the cleavage sites turn into surface states (Fig. 4.2) [45, 48]. The band structure of bilayer Ca_2N demonstrates the clear separation between the interstitial states, which retain their bulk character, and the higher-energy surface states. Calculations involving multiple layers of Ca_2N (Fig. 4.3) reveal an extra interstitial state for each additional interstitial gap. In the case of a monolayer, there are only surface states. These states form distinct bonding and anti-bonding combinations that are non-degenerate. However, with the addition of more layers, the surface states experience less coupling due to an increased spatial separation and tend towards degeneracy [46, 75]. The presence of these surface states (green) is clear from the ILDOS plot in Fig. 4.2. The lower density (0.5 e per Ca_2N unit) seen for the surface states reflects their reduced stability relative to the interstitial states (1 e per Ca_2N unit). It is also notable that the density of the surface states is higher for the monolayer than the bilayer, which reflects the greater depth of the 'bonding' surface state below the FL for the monolayer.

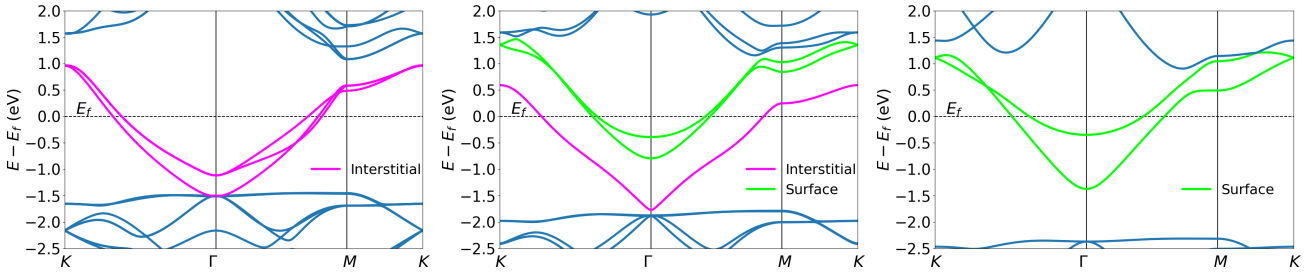

(a) Bulk Ca_2N (hexagonal cell) (b) Bilayer Ca_2N (c) Monolayer Ca_2N

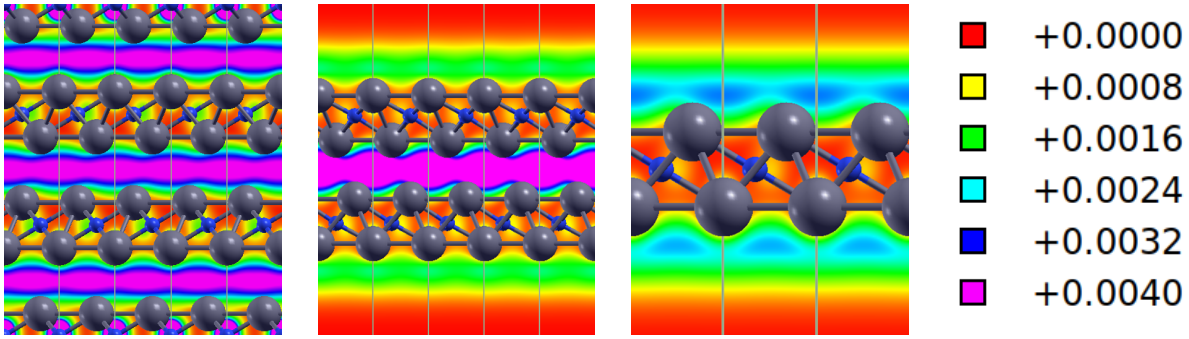

(d) Bulk Ca_2N (hexagonal cell) (e) Bilayer Ca_2N (f) Monolayer Ca_2N (g) Color scale

Figure 4.2: Ca_2N band structures (top) for the bulk hexagonal cell (left), bilayer (middle), and monolayer (right), with the interstitial and surface states highlighted. Also shown are heat maps (bottom) of the integrated local density of states (ILDOS) in the xz-plane, for an energy range between -1.0 eV and the FL (E_f). The color scale runs from isodensity values of 0 (red) to 0.004 a.u. (purple).

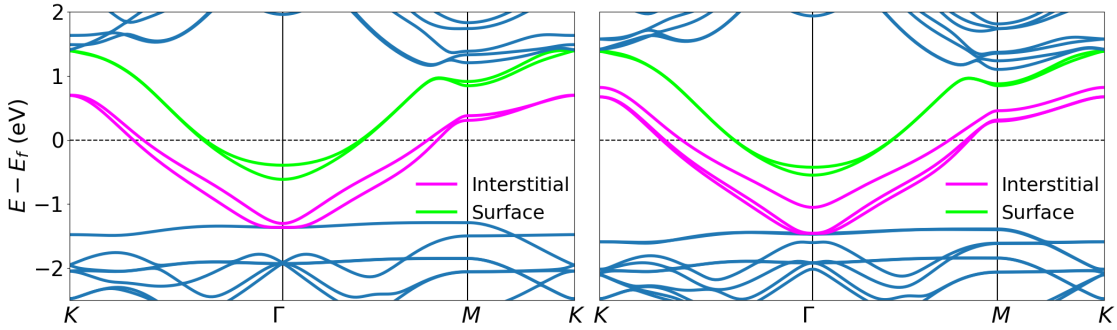

Figure 4.3: Ca_2N band structure for trilayer (left) and quadlayer (right), with interstitial and surface states highlighted.

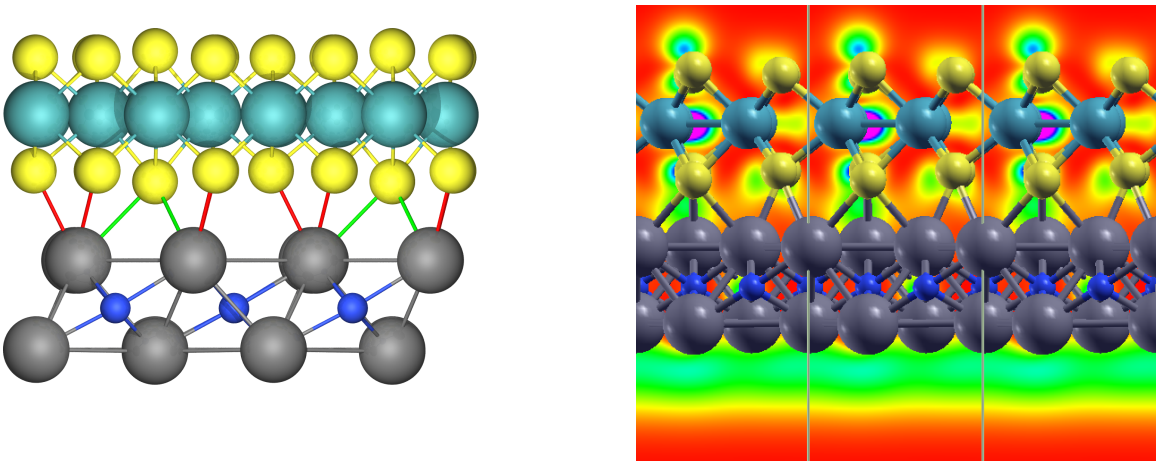

Figure 4.4: Structure of Ca_2N–MoS_2 interface in the xz-plane, indicating both short (red) and long (green) S–Ca bonds. The ILDOS in the yz-plane for an energy range between -1.0 eV and the Fermi level is also shown. The isodensity values used for the color scale match those in Figure 4.2.

4.3.2 The Ca_2N–MoS_2 Interface

The most energetically favourable configuration of the Ca_2N–MoS_2 interface is shown in Figure 4.4. The optimal orientation was obtained by performing a scan of the total energy as a function of displacement along the diagonals of the cell (Fig. 4.5). The structure contains two distinct types of S–Ca bonds. Three of the four sulfur atoms have tetrahedral coordination and form close contacts with a single calcium atom, with a bond length of 2.68 Å.

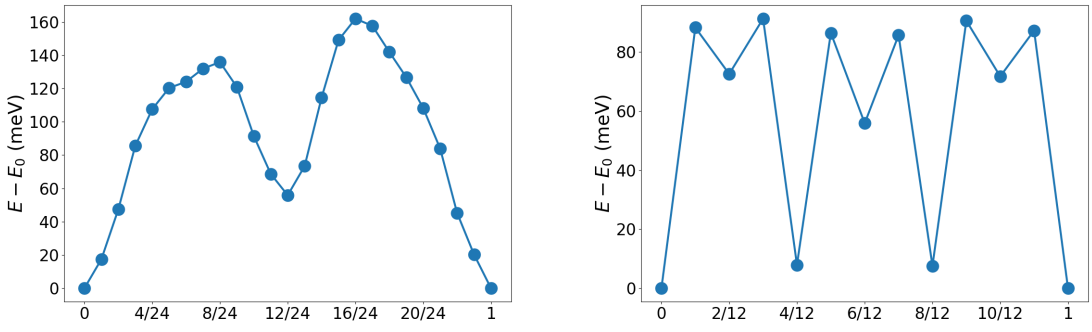

(a) (b)

Figure 4.5: Potential energy surfaces for sliding along the a) long and b) short diagonals of the Ca_2N–MoS_2 cell. The energy is expressed relative to the minimum.

The fourth, hypervalent sulfur atom has octahedral coordination and forms contacts to three calcium atoms, each with bond lengths of 2.95 Å. Both of these values are well within the sum of vdW radii. Each of the calcium atoms at the interface forms one short and one long bond to a sulfur.

Formation of the Ca_2N–MoS_2 heterostructures is quite favourable energetically, with the exfoliation energy as a function of the number of Ca_2N layers shown in Table 4.2. Due to the higher reactivity of the Ca_2N monolayer, resulting from the lack of any interstitial states, the exfoliation energy for the $N = 1$ heterostructure is slightly higher than for the $N = 2$, which already approximates the bulk limit. Dispersion interactions only account for 35-37% of the exfoliation energy, indicating that charge transfer is primarily responsible for the Ca_2N–MoS_2 bonding. In agreement with previous results [40, 51, 52], formation of the interface causes significant distortion to the MoS_2 monolayer (Fig. 4.4), while the geometry of the electride layer is largely unperturbed. This is quantified by the distortion energies given in Table 4.2.

Table 4.2: Computed exfoliation energies (E_{exfol}) for Ca_2N–MoS_2 heterostructures with varying numbers of electride layers, N. The XDM dispersion contributions are shown in parentheses. The distortion energies (E_{dist}) for the MoS_2 monolayer and Ca_2N are also given. All quantities are in meV/Å^2.

N	E_{exfol}	$E_{\text{dist}}(MoS_2)$	$E_{\text{dist}}(Ca_2N)$
1	88 (31)	28	3
2	82 (30)	22	2
3	83 (31)	22	2
4	83 (31)	22	2

In order to better understand how the formation of the interface influences the electronic states of both MoS_2 and Ca_2N, we carry out a side-by-side comparison of the band structures (Fig. 4.6) of the materials before (left) and after (right) coming into contact. This is performed for the case of monolayer Ca_2N (top) and bilayer Ca_2N (bottom) to examine how both surface and interstitial anion electron states are affected. The effects of the MoS_2 geometric distortion can be seen in the band structures in Fig. 4.6. Relative to the isolated materials, formation of the heterostructures results in significant modification of the valence and conduction bands of MoS_2, accompanied by a reduction in the band gap. The most notable change to the Ca_2N band structure is the withdrawal of one of the surface states upwards in energy.

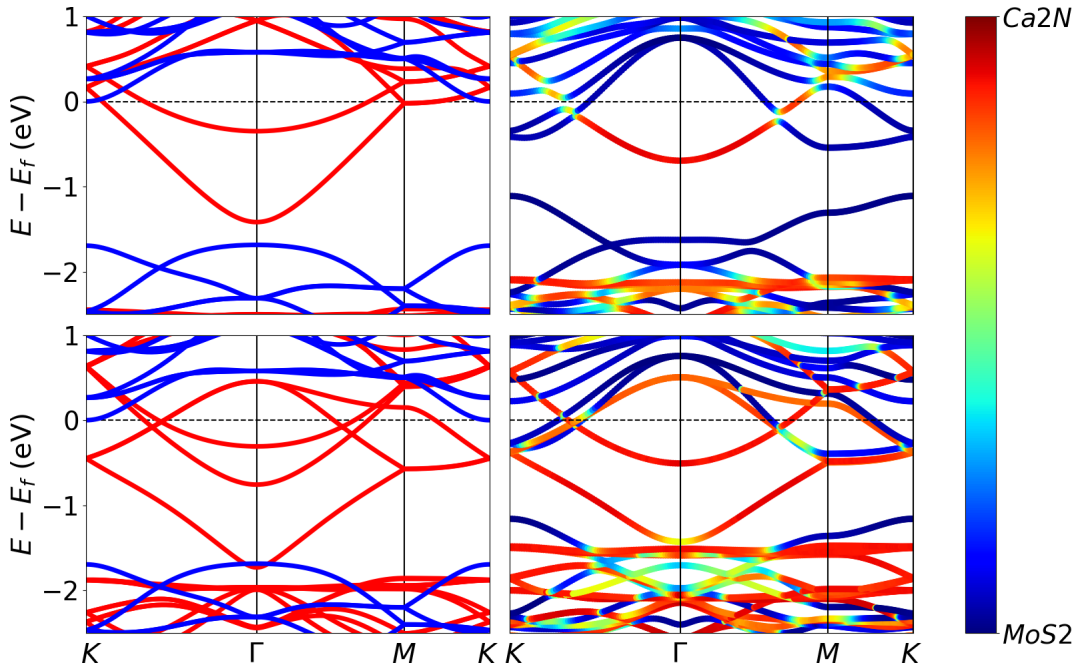

Figure 4.6: Band structure modifications resulting from formation of interfaces between MoS_2 and monolayer (top) or bilayer (bottom) Ca_2N. The plots on the left show an overlay of the band structures for the relaxed isolated materials, with fixed lattice constants matching that of the interface. The plots on the right show the band structures for the resulting interfaces, colored based on orbital contributions from the two materials at each **k**-point.

The absence of one surface state is expected from the ILDOS shown in Figure 4.4, as formation of the heterostructure eliminates the Ca_2N surface state nearest to the interface. The remaining surface state in the band structure corresponds to the anionic electrons on the surface opposite the interface, as seen in the ILDOS. The electrons from the missing Ca_2N surface state are donated to the MoS_2 and, consequently, we see little band mixing between the materials due to the ionic nature of the interface. The same behaviour is observed when three and four layers of Ca_2N are interfaced with MoS_2 (Fig. 4.7). All significant features remain, with the presence of an additional interstitial electride state per each new Ca_2N layer. This suggests that the contribution from Ca_2N layers away from the interface quickly drops after the first layer. This leads us to conclude that nearly all properties of the interface are due to the presence of a single Ca_2N layer, while additional layers do not play a major role in the interaction with MoS_2.

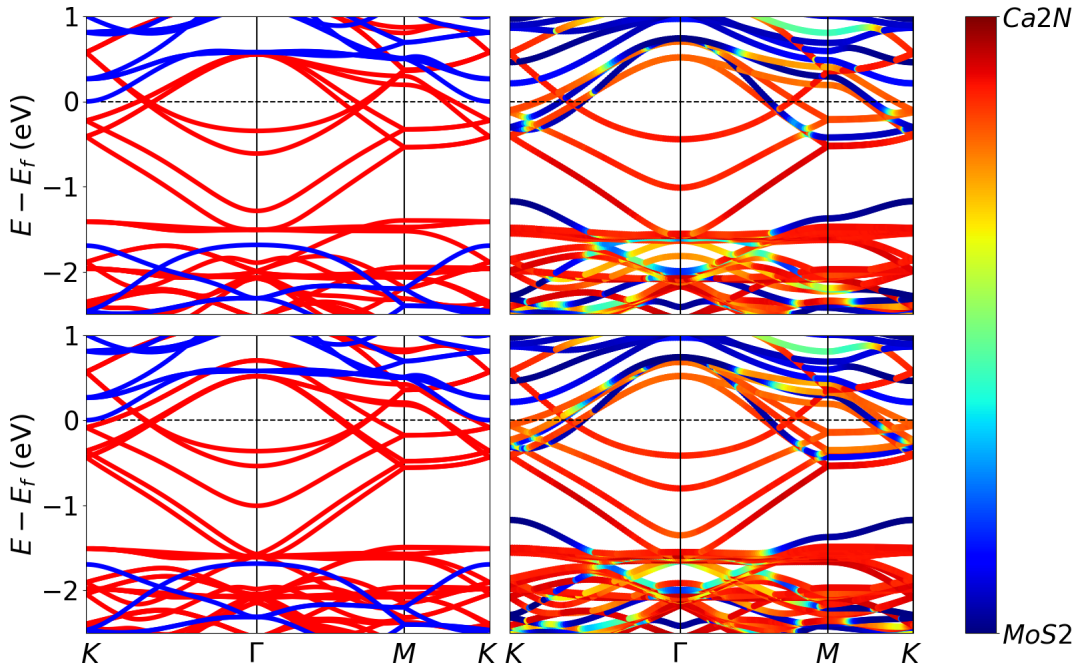

Figure 4.7: Band structure modifications resulting from formation of interfaces between MoS_2 and 3-layer (top) or 4-layer (bottom) Ca_2N. The plots on the left show an overlay of the band structures for the relaxed isolated materials, with fixed lattice constants matching that of the interface. The plots on the right show the band structures for the resulting interfaces, colored based on orbital contributions from the two materials at each **k**-point.

The gradual disappearance of the Ca_2N surface state can be observed by varying the distance between Ca_2N and MoS_2 from equilibrium and calculating the consequent band structures. Fig. 4.8 shows the band structures of the Ca_2N–MoS_2 interface, showing the component contributions from each material at several interlayer distances. The atomic positions were held constant at their equilibrium positions and only their relative out-of-plane distance was varied. That is why, even at large interlayer distances with weak interactions, the shape of the MoS_2 bands remains distorted relative to its pristine state. As the two layers are pulled apart, the interaction between them weakens and the missing surface state starts to reappear from above the FL. This is accompanied by decreased doping of MoS_2, as can be seen by the shift in its CBE towards the FL. At the distance of $d_0 + 5$ Å, the interaction is very weak. We see the missing surface state is almost completely restored to its pre-interfaced state and the MoS_2 is almost undoped, with its CBE near the FL.

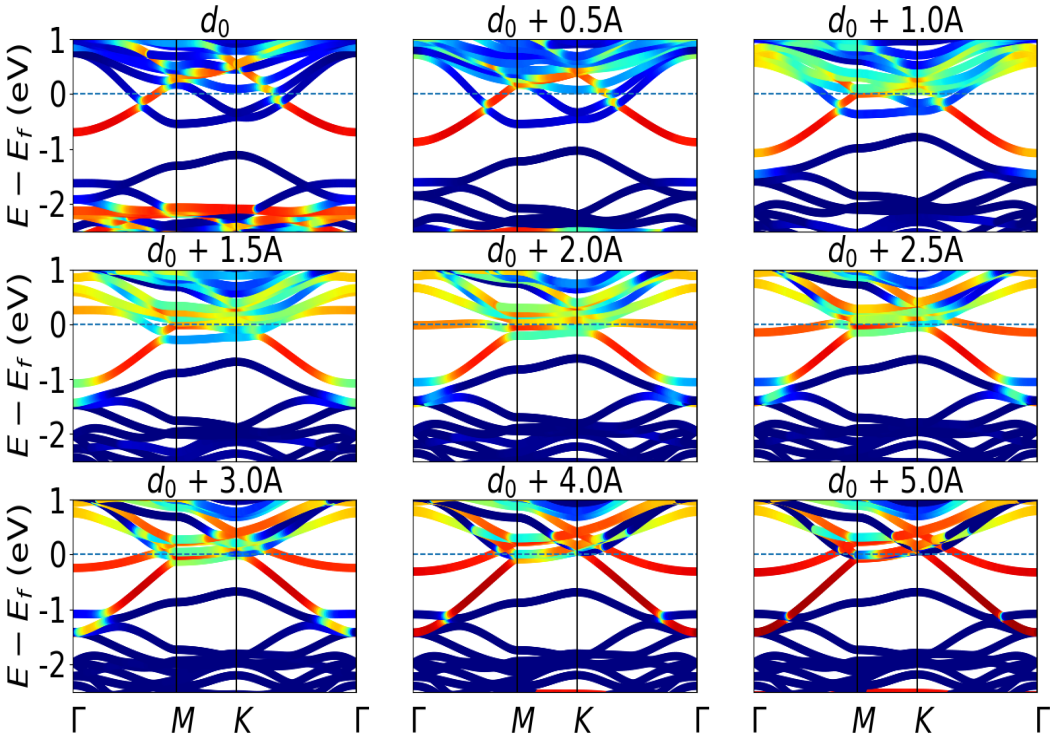

Figure 4.8: Band structures of monolayer Ca_2N–MoS_2 heterostructures calculated at varying distances relative to the equilibrium distance, d_0, in order to highlight the effects of the interaction between the two materials. The states are coloured based on orbital contributions, with contributions from Ca_2N in red and contributions from MoS_2 in blue.

From the Bader charge difference (Fig. 4.9), we estimate a transfer of 0.35 electrons per MoS_2 formula unit (or 0.47 electrons per Ca_2N formula unit), comparable to that seen for the Ca_2N–$MoTe_2$ heterostructure [40, 51]. Fig. 4.9 also indicates that the addition of more Ca_2N layers slightly decreases the amount of charge transfer to MoS_2. This is likely due to the presence of interstitial sites not present in the monolayer case, which provide an alternative and relatively stable space for electrons to occupy. Note that the amount of charge transfer quickly converges to bulk behaviour after the addition of a second Ca_2N layer. The transfer of roughly half an electron from $[Ca_2N]^+(e^-)$ is consistent with the loss of one of the two surface states. The high charge transfer results in the metalization of the MoS_2 bands in Fig. 4.6, with the drop of the conduction band edge to 0.54 eV below the FL. This is much greater than the drop reported by Dhakal et al. in their calculations for doped bilayer MoS_2 ($\approx$90 meV) [52]. The discrepancy possibly indicates more charge transfer in the monolayer

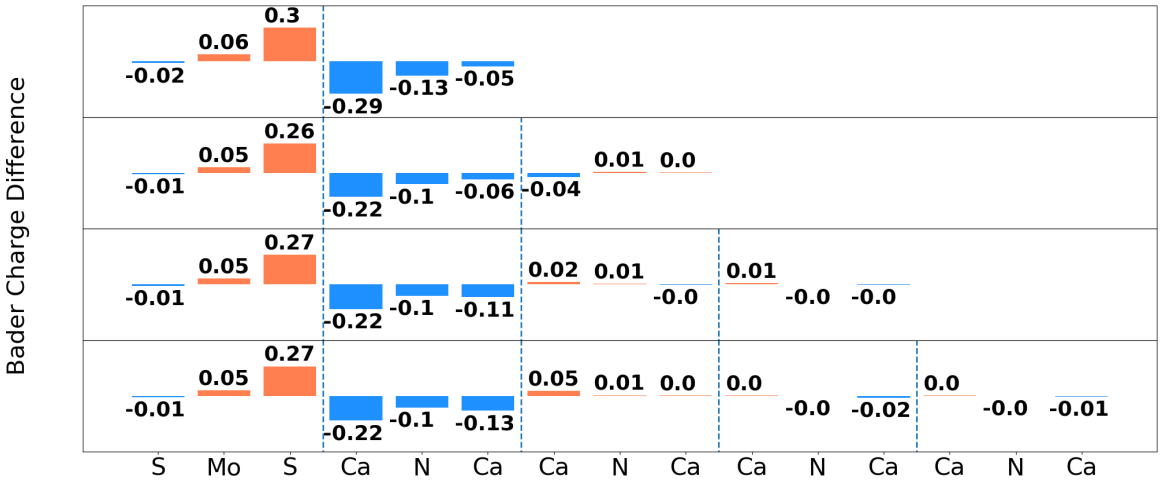

Figure 4.9: Differences in Bader atomic charges for the various Ca_2N–MoS_2 interfaces, relative to the separated materials. Positive (negative) values indicate accumulation (depletion) of electron density.

TMDC case; however, it is more likely due to those authors' omission of structural changes to the MoS_2. The metallic nature of the interface indicates the absence of a Schottky Barrier.

Figure 4.10 shows the average out-of-plane electrostatic potential for heterostructures with multiple layers of Ca_2N. As expected from the exfoliation energy data, convergence to the bulk limit is already seen for the bilayer case. The average potential is slightly below the Fermi energy, indicating the absence of a tunnelling barrier. However, the average value does not convey the full picture. The electrostatic potential is very anisotropic and covers a wide range of values as indicated by the red bar in the figure. Fig. 4.11 shows a heatmap of a slice of the electrostatic potential at the maximum value of the average out-of-plane potential between Ca_2N and MoS_2. Clearly, the majority of the energy potential landscape is below the FL and, thus, presents no barrier to incoming electrons. The most negative values occur about the single, octahedrally coordinated sulfur. Thus, the Ca_2N–MoS_2 interface is barrier-free, further illustrating the ohmic nature of the contact.

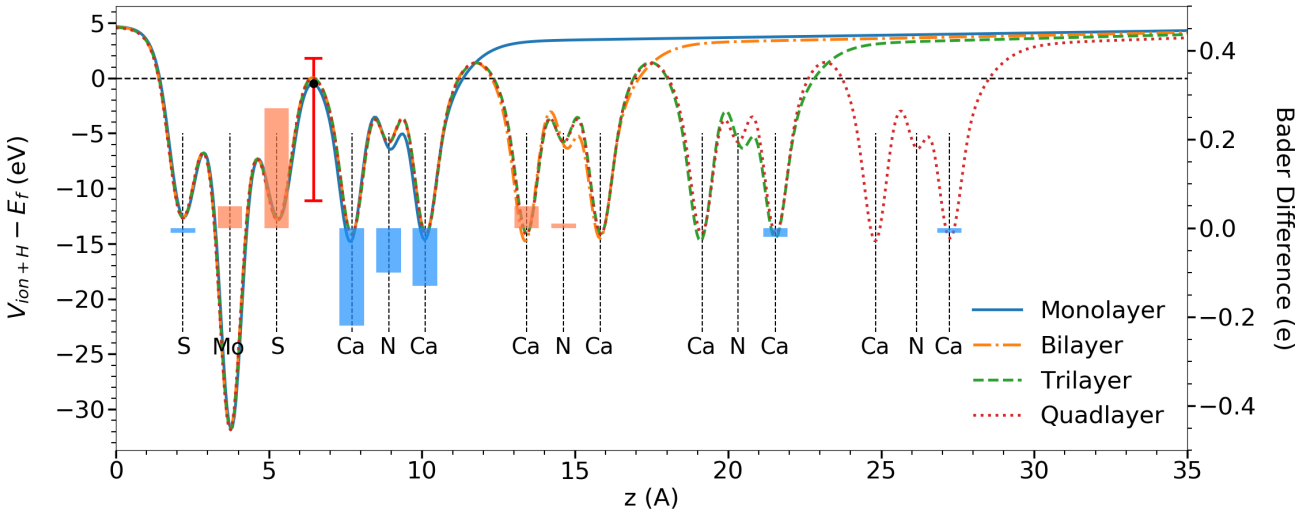

Figure 4.10: Out-of-plane average of the electrostatic potential (sum of the ionic and Hartree potentials) for various Ca_2N–MoS_2 interfaces. The red bar indicates the range of values at the maximum point within the interface region. The results are overlaid with the difference in Bader atomic charges for the 4-layer Ca_2N–MoS_2 interface, relative to the separated materials. Positive (negative) values indicate accumulation (depletion) of electron density.

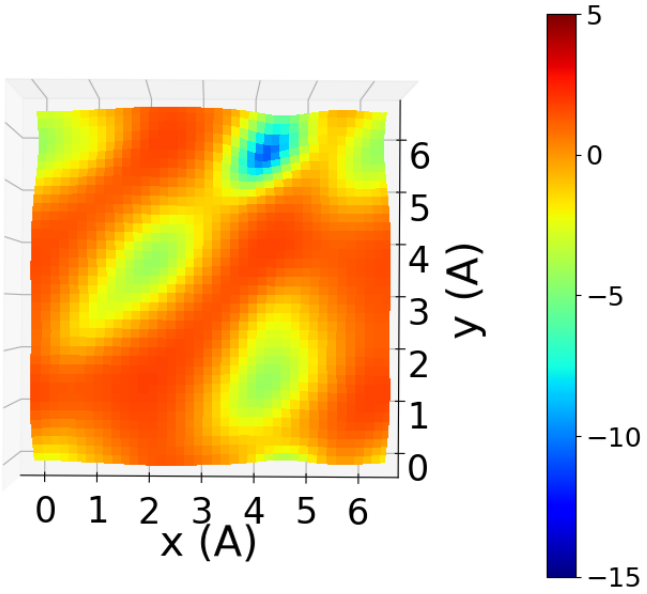

Figure 4.11: Electrostatic potential surface at the Ca_2N–MoS_2 interface in the xy-plane. The chosen point in the z-direction corresponds to the maximum value of the average out-of-plane electrostatic potential (black point in Fig. 4.10).

4.3.3 The Au–Ca_2N–MoS_2 Interface

Finally, the benefits of inserting a single layer of Ca_2N at a real device contact are investigated. We choose the well-studied Au–MoS_2 interface, which is known to exhibit poor electrical conductance due to the presence of a vdW gap [10, 11, 12, 17]. Results for both the Au–MoS_2 and Au–Ca_2N–MoS_2 heterostructures are presented to assess the advantages of adding an interfacial layer of Ca_2N.

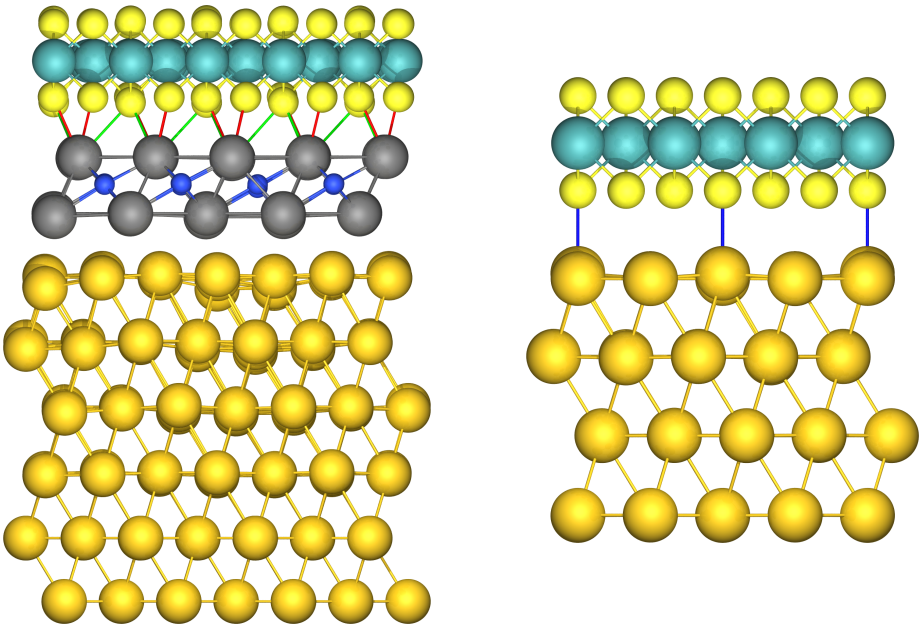

(a) Au–Ca_2N–MoS_2 (b) Au–MoS_2

Figure 4.12: Geometries of the relaxed Au–Ca_2N–MoS_2 and Au–MoS2 heterostructures. The short and long S–Ca contacts are shown in red and green, respectively, while the shortest S–Au contacts are shown in blue.

Fig. 4.12 shows the geometry of the relaxed Au–MoS_2 heterostructure, with and without an inserted layer of the Ca_2N electride. The Ca_2N–MoS_2 bonding motifs, discussed in the previous section, are not affected by the presence of the Au surface. However, the lengths of the short S–Ca bonds are slightly increased, to $2.75 - 2.78$ Å, while the lengths of the long S–Ca bonds are increased to $3.06 - 3.15$ Å. This implies that the presence of the Au surface may slightly weaken the ionic bonding between Ca_2N and MoS_2. In order to determine the optimal orientation, we calculate the total energy as a function of displacement along the diagonals (Fig. 4.13). The difference in interaction strength between Au and Ca_2N or MoS_2 is highlighted by the stark

difference between the sliding potentials. The Au–Ca_2N interaction is ionic in nature and is three orders of magnitude greater than the vdW bonding between Au and MoS_2.

The exfoliation energies for the two heterostructures are given in Table 4.3. For Au–MoS_2, the dispersion contribution is slightly greater than the total exfoliation energy (due to non-bonded repulsion from the base density functional), confirming the vdW nature of the interface. There is also no significant distortion of either the MoS_2 monolayer or Au surface. For Au–Ca_2N–MoS_2, the tabulated exfoliation energy corresponds to the energy relative to the separate Au surface, Ca_2N and MoS_2 monolayers. Inserting the Ca_2N layer markedly increases the total exfoliation energy, by roughly a factor of 8, and dispersion is now responsible for only 27% of the exfoliation energy. This confirms that, as for Ca_2N–MoS_2, charge transfer is the dominant stabilizing interaction for Au–Ca_2N–MoS_2. There is again significant distortion of the MoS_2 monolayer, albeit to a lesser extent than for Ca_2N–MoS_2 without the Au surface. Insertion of the electride also results in visible distortion of the Au surface, as seen in Fig. 4.12. However, due to its soft metallic nature, the energy penalty accompanying this distortion is minor.

Table 4.3: Computed exfoliation energies (E_{exfol}) for the Au–MoS_2 and Au–Ca_2N–MoS_2 interfaces. The XDM dispersion contributions are shown in parentheses. The distortion energies (E_{dist}) for the Au surfaces and the Ca_2N and MoS_2 monolayers are also given. All quantities are in meV/Å^2.

Quantity	Au–MoS_2	Au–Ca_2N–MoS_2
E_{exfol}	31 (36)	256 (70)
E_{dist}(Au)	0	1
E_{dist}(Ca_2N)	—	3
E_{dist}(MoS_2)	0	16

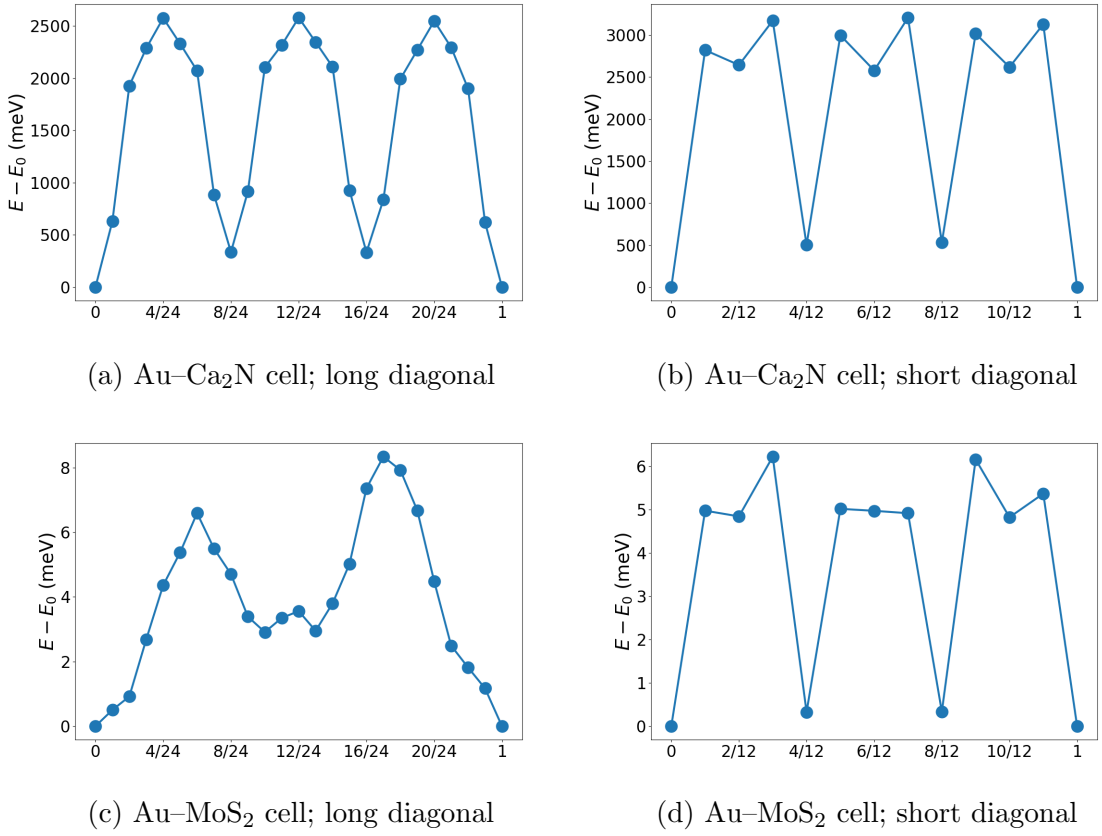

(a) Au–Ca_2N cell; long diagonal

(b) Au–Ca_2N cell; short diagonal

(c) Au–MoS_2 cell; long diagonal

(d) Au–MoS_2 cell; short diagonal

Figure 4.13: Potential energy surfaces for sliding along the long and short diagonals of the Au–Ca_2N and Au–MoS_2 cells. The energy is expressed relative to the minimum.

The band structure predicted for the Au–Ca_2N–MoS_2 is shown in Fig. 4.14, with the band structure for the reference Au–MoS_2 interface shown in Fig. 4.15. For the Au–MoS_2 interface, the band structure reveals strong Fermi-level pinning, with the MoS_2 conduction band edge pinned 0.6 eV above the FL. As expected, we also see virtually no distortion to either the MoS_2 or Au bands. Bader charge analysis (Fig. 4.17) indicates virtually no charge transfer between the metal and TMDC, as expected for a vdW contact. Conversely, for the Au–Ca_2N–MoS_2 heterostructure, the MoS_2 bands are significantly modified due to a combination of geometric distortion and doping. The band structure in Fig. 4.14 does not show any Ca_2N surface states near the FL, as the anionic electrons occupying these states have been donated to the MoS_2 and Au at both sides of the interface. The ionic nature of the interface results in the absence of band mixing. Bader charge analysis (Fig. 4.17) confirms charge transfer of 0.79 electrons per Ca_2N formula unit. Although the net negative charge

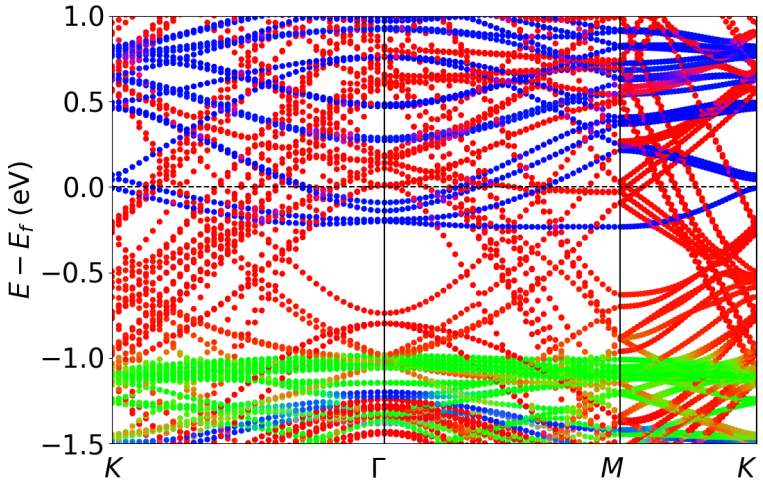

Figure 4.14: Band structure of the Au–Ca_2N–MoS_2 heterostructure. The orbital contributions, summed over atoms forming each material, were used to assign the RGB color vector (red: Au, green: Ca_2N, blue: MoS_2) for each **k**-point.

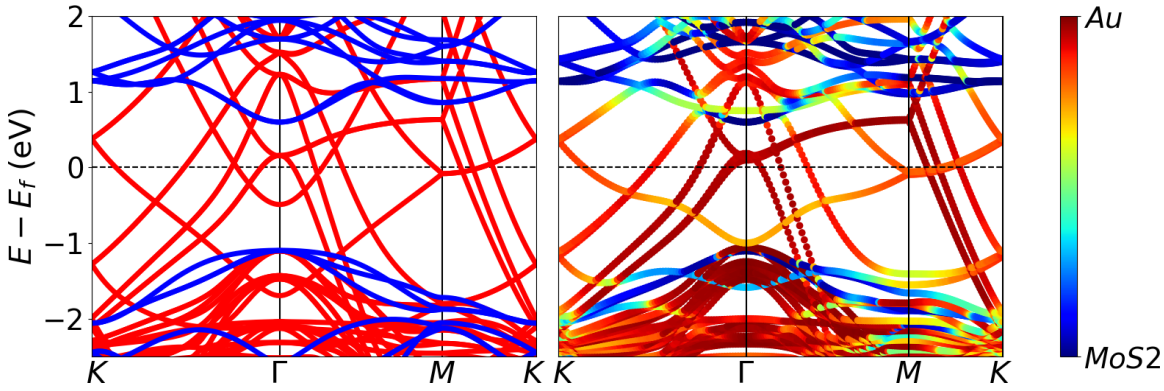

Figure 4.15: Band structure modifications resulting from formation of the Au–MoS_2 interface. The plot on the left shows an overlay of the band structures for the relaxed isolated materials, with fixed lattice constants matching that of the interface. The plot on the right shows the band structures for the resulting interface, colored based on orbital contributions from the two materials at each **k**-point.

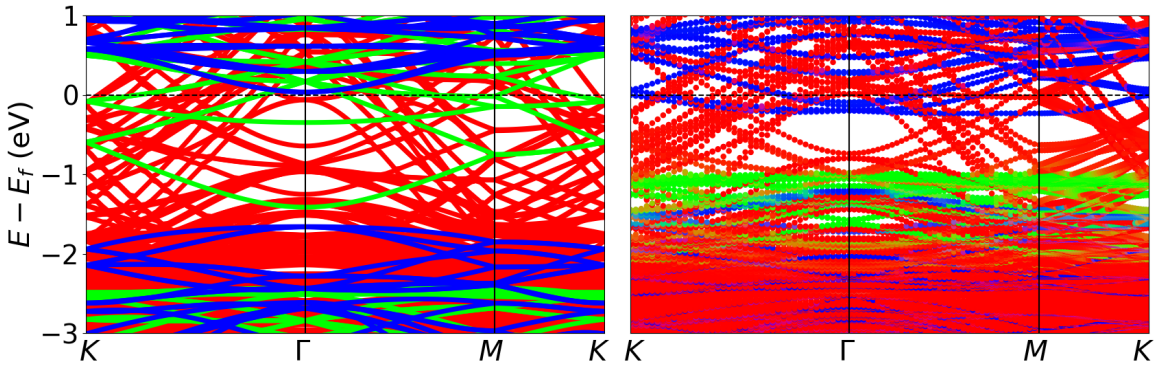

Figure 4.16: Band structure modifications resulting from formation of the Au–Ca_2N–MoS_2 interface. The plot on the left shows an overlay of the band structures for the relaxed isolated materials, with fixed lattice constants matching that of the interface. The plot on the right shows the band structures for the resulting interface. The orbital contributions, summed over atoms forming each material, were used to assign the RGB color vector (red: Au, green: Ca_2N, blue: MoS_2) for each **k**-point.

on MoS_2 (0.26 electrons per formula unit) is reduced compared to the isolated Ca_2N–MoS_2 heterostructure, the charge transfer is still significant enough to drop the conduction band edge 0.23 eV below the FL. Insertion of the electride metallizes the MoS_2 bands and eliminates the Schottky barrier.

Similar to what was done in Figures 4.6, 4.7, and 4.15, we perform a side-by-side comparison of bands structures of Au, Ca_2N and MoS_2 before and after the formation of the heterostructure. The left panel of Fig. 4.16 shows the overlayed band structures of the three pristine materials before coming into contact and the right panel shows the band structure of the fully-formed interface. Note that the right panel of Fig. 4.16 shows the same band structure as in Fig. 4.14, but with a larger energy range along the y-axis. The extended energy range was chosen to make the MoS_2 valence bands visible in the left panel of the figure. The low energy MoS_2 bands are not quite visible in the right frame due to the overwhelming presence of the Au bands. Fig. 4.16 clearly illustrates the missing electride surface states, whose electrons have been donated to the TMDC and metal. We also note the same significant distortion of the MoS_2 bands and band gap, as well as the drop of the CBE below the FL at M.

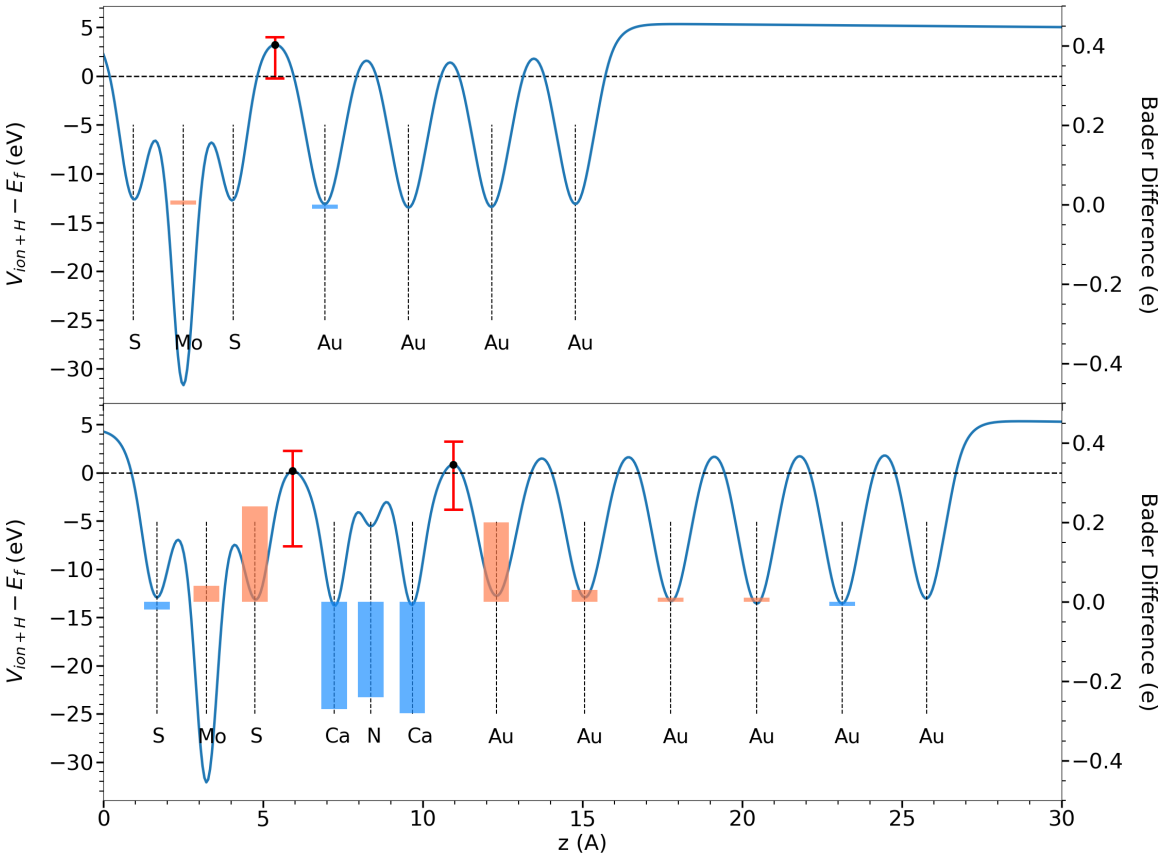

Figure 4.17: Out-of-plane average of the electrostatic potential (sum of the ionic and Hartree potentials) for the Au–MoS_2 (top) and Au–Ca_2N–MoS_2 (bottom) interfaces. The red bars indicate the range of values at the maximum point within the interface regions. The results are overlaid with the differences in Bader atomic charges for the heterostructures, relative to the separated materials. Positive (negative) values indicate accumulation (depletion) of electron density.

The electrostatic potentials for the Au–MoS_2 and Au–Ca_2N–MoS_2 heterostructures are compared in Fig. 4.17. Typical of a vdW contact, the maximum of the electrostatic potential at the Au–MoS_2 interface is a few eVs above the FL, with the majority of values at that point lying above the FL as well. This results in a considerable tunnelling barrier for injected electrons, making it extremely difficult to establish proper electrical contact. However, the presence of Ca_2N between the metal and TMDC reduces the average potential barrier at both sides of the interface. Although the maximum values at the interfaces are still positive, local values of the potential now extend well below the FL for both interfaces, making it significantly easier for injected electrons from the metal contact to make their way through to the

TMDC. Fig 4.18 shows heat maps of the electrostatic potential between the various interfaced materials for both the Au–MoS_2 and Au–Ca_2N–MoS_2 heterostructures. Comparing with Fig 4.11, we see that the presence of a metal contact on the other side of Ca_2N only slightly affects the potential landscape at the Ca_2N–MoS_2 interface. Of greater interest, in the absence of Ca_2N, the potential landscape at the Au–MoS_2 interface is almost completely above the FL, creating a significant barrier. However, after inserting Ca_2N, the potential at the interface with the metal contains significant regions where the potential is below the FL, which makes it easy for charge carriers to pass through.

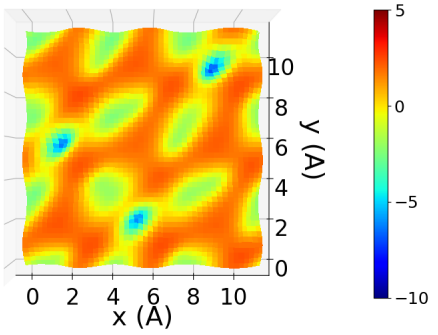

(a) Potential surface across the Ca_2N–MoS_2 interface in the Au–Ca_2N–MoS_2 heterostructure

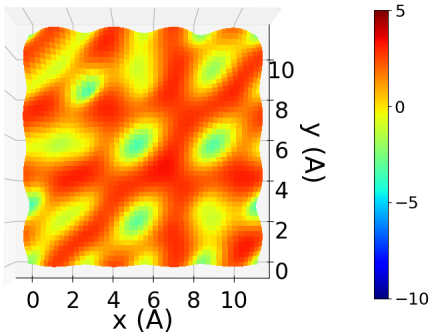

(b) Potential surface across the Au–Ca_2N interface in the Au–Ca_2N–MoS_2 heterostructure

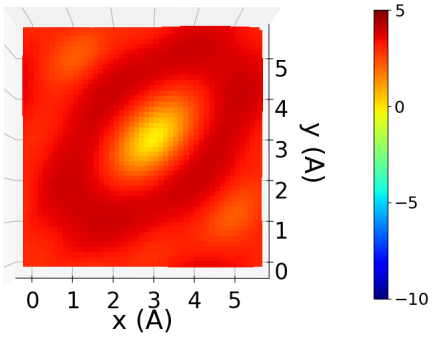

(c) Potential surface across the Au–MoS_2 interface in the Au–MoS_2 heterostructure

Figure 4.18: Electrostatic potential surfaces in the xy-plane between different materials in the Au–Ca_2N–MoS_2 and Au–MoS_2. The chosen points in the z-direction correspond to the maximum values of the average out-of-plane electrostatic potentials (black points in Fig. 4.17).

4.4 Summary

Using dispersion-corrected DFT, we identified the interstitial electronic states in bulk Ca_2N and their transformation to surface states after exfoliation. The surface states play a critical role in determining the properties of heterostructures of Ca_2N with MoS_2 or Au, as the excess electrons occupying these states are donated to the interfaced material. In the case of the Au–Ca_2N–MoS_2 heterostructure, the resulting doping of the MoS_2 layer is enough to bring its conduction band edge below the FL, creating a contact that is free of both tunnelling and Schottky barriers. We also find considerable doping of the metal by the electride, which is likely magnified for Au compared to other metals due to its high electronegativity. Our results suggest a promising solution to the metal-TMDC contact problem.

Chapter 5

Conclusion

It is extremely likely that 2D layered materials will take on a significant role in the future of the electronics industry due to the large global effort to study and characterize them, with the goal of practical application. 2D materials have shifted the way we understand and look at solid-state systems. When isolated into a single layer, relatively mundane bulk materials can suddenly display exotic electronic properties. It is thought that monolayer TMDCs will play an important part in 2D devices as they are stable in ambient conditions and display a wide variety of properties from metallic to semiconducting and insulating. In chapter 1 we introduced MoS_2, a TMDC that has attracted the attention of the community due to its diverse field of applications. In particular, MoS_2 shows great promise in use for photodetectors, solar cells, chemical sensors and low-power transistor devices, and may even one day displace Si as the industry standard. However, despite the interest and potential, MoS_2-based technology has yet to penetrate into the mainstream. MoS_2 lacks any out-of-plane dangling bonds. This makes it difficult to establish proper electrical contact with a metal, a requirement for any practical device. Most interfaces between MoS_2 and *d*-block transition metals are plagued by high tunnelling and Schottky barriers and exhibit strong Fermi-level pinning. In order to achieve the desired ohmic contact, all of these issues must be resolved. Chapter 1 also introduced the notion of electrides, a family of ionic materials with an excess of electrons. Of particular importance to this work is Ca_2N, one of the two known 2D layered electrides. In exfoliated Ca_2N, the excess electrons reside at the surface and are characterized by a nearly-free and delocalized nature. These surface states are highly reactive and allow Ca_2N to bind strongly to other surfaces. This has been demonstrated here by inserting Ca_2N at a metal-MoS_2 interface in order to overcome the challenge of forming a good electrical contact.

Chapter 2 discusses the theory and methods behind the calculations used in this

work. Starting with the structure of electronic states in periodic solids, section 2.1 first presents the many-body Hamiltonian and explains how its symmetry and periodicity can be exploited to simplify the path to its solution. Section 2.2 follows by outlining the basic principles of Kohn-Sham DFT and ends with a brief discussion of the XDM dispersion model. The rest of the chapter is dedicated to sketching the under-the-hood workings of the computational methods used to solve the KS equations (the PAW method), as well as the methods used to obtain our results (state projection and Bader charge transfer). All calculations in this work were conducted within a DFT framework using Quantum ESPRESSO [53]. This includes the post-processing calculations used to determine various charge densities, potentials, and projections of states, with the exception of the Bader charge differences, which were determined using the critic2 code [81].

Chapter 3 shows the preliminary convergence tests to determine optimum computational parameters, as well as potential energy curves used to identify the equilibrium lattice constants for Ca_2N, MoS_2, and Au. Traditionally, the process of optimizing lattice constants is automated within Quantum ESPRESSO. However, due to our choice of the XDM dispersion model, this had to be done manually. This is due to the assumption of static dispersion coefficients in evaluation of cell stresses in the XDM implementation. This assumption has no effect on the overall accuracy of XDM, but remains an outstanding problem with the current implementation.

Chapter 4 includes the numerical details of the Quantum ESPRESSO calculations, as well as specifics on how the unit cells for each interface were constructed and a list of their dimensions; cells containing more than one material adopted the cell size of MoS_2. The results were presented beginning with the evolution of the Ca_2N electride states for a gradual transition from bulk to monolayer. These interstitial and surface states are the only ones within a large energy range around the FL and are easily identifiable on plots of the band structure. Due to the strong shielding between layers, the sequential addition of more layers is easily tracked with the appearance of a new interstitial state per each new layer. This also results in a quick convergence to bulk behaviour, as can be seen in the charge donation trends and average out-of-plane potentials. The surface states are highly reactive. Interfacing Ca_2N with MoS_2 results in a complete depletion of the surface state electrons into the MoS_2. This

lowers MoS_2's conduction band edge below the FL, metalizing the semiconductor and eliminating the Schottky barrier. Again, the work here greatly benefits from the ease of interpretability of Ca_2N's band structure as we clearly see the disappearance of a surface state upon contact with MoS_2.

The comparative study of the Au–MoS_2 heterostructure with and without insertion of Ca_2N clearly demonstrates the potential benefits of inserting an electride at a metal–TMDC interface. Au was chosen due to its ubiquitous use in industry and well-documented poor contact with MoS_2. Our results confirmed that the Au–MoS_2 interface is a vdW contact afflicted with strong Fermi-level pinning, as well as high tunnelling and Schottky barriers. Introducing Ca_2N to the junction effectively remedies all these issues. The electride surface states are readily donated to both the metal and TMDC, flooding both with an excess of electrons that removes the Schottky barrier and binds the materials together with strong ionic bonding. Bader charge differences show the virtually complete depletion of the surface states; however, this can also clearly be seen from the disappearance of the Ca_2N surface states in the band structure of the Au–Ca_2N–MoS_2 heterostructure. The average electrostatic potential across the interface shows marked improvement with the introduction of Ca_2N. Most notably, the potential landscape now has energy valleys much lower than the FL, creating an accessible path for injected electrons.

The work presented here serves as a proof-of-concept. The insertion of Ca_2N at the Au–MoS_2 interface completely transforms the nature of the contact from vdW to ohmic. This success may indicate the more general benefit of inserting a 2D electride at a metal–TMDC interface. Future work should study different combinations of metal–electride–TMDC heterostructures to gain a more holistic perspective on how the three materials interact. A natural next step would be to replace Au with Ag or Cu in order to understand how interactions with Ca_2N would trend down the same group of the periodic table. It is likely that the results would be qualitatively similar, but with less charge transfer to Ag and Cu due to their decreased electronegativity compared to Au. Not all metals form vdW contacts with MoS_2 like the noble metals do. Other transition metals, like Ti and Mo, are known to form stronger bonds with MoS_2 due to a greater orbital overlap [11, 15, 16]. Although these contacts are not held together by vdW forces, they still exhibit Fermi-level pinning and form Schottky

barriers. The presence of Ca_2N may enhance such interfaces to an even greater degree compared to contacts with noble metals and other non-noble metals. Heterostructures with magnetic metals, such as Ni, are also a source of interest. A Ni–Ca_2N interface may lead to a spin-polarized current with potential applications in spintronic devices.

It is clear that new applications of 2D electrides may help solve old problems and open doors to many potential opportunities. As of today, Ca_2N and Y_2C are the only 2D electrides that have been successfully synthesized as single crystals, but structures of many others have been proposed computationally [84]. These electron-rich materials may have arrived at just the right time to advance the promising field of 2D materials.

Appendix A

Permission to Reuse Figure

SPRINGER NATURE LICENSE
TERMS AND CONDITIONS

Jun 10, 2021

This Agreement between Mr. Fouad Kaadou ("You") and Springer Nature ("Springer Nature") consists of your license details and the terms and conditions provided by Springer Nature and Copyright Clearance Center.

License Number	5085390688783
License date	Jun 10, 2021
Licensed Content Publisher	Springer Nature
Licensed Content Publication	Nature
Licensed Content Title	Dicalcium nitride as a two-dimensional electride with an anionic electron layer
Licensed Content Author	Kimoon Lee et al
Licensed Content Date	Jan 30, 2013
Type of Use	Thesis/Dissertation
Requestor type	academic/university or research institute
Format	electronic
Portion	figures/tables/illustrations
Number of figures/tables/illustrations	1

High-res required	no
Will you be translating?	no
Circulation/distribution	1 - 29
Author of this Springer Nature content	no
Title	Improved charge transport across metal-MoS2 interface through the insertion of 2D electride Ca2N
Institution name	Dalhousie University
Expected presentation date	Aug 2021
Portions	Figure 1.a
Requestor Location	5245 Smith St Unit 1 Halifax, NS B3H 1M3 Canada Attn: Fouad Kaadou
Total	0.00 CAD

Terms and Conditions

Springer Nature Customer Service Centre GmbH
Terms and Conditions

This agreement sets out the terms and conditions of the licence (the **Licence**) between you and **Springer Nature Customer Service Centre GmbH** (the **Licensor**). By clicking 'accept' and completing the transaction for the material (**Licensed Material**), you also confirm your acceptance of these terms and conditions.

1. Grant of License

1. 1. The Licensor grants you a personal, non-exclusive, non-transferable, world-wide licence to reproduce the Licensed Material for the purpose specified in your order only. Licences are granted for the specific use requested in the order and for no other use, subject to the conditions below.

1. 2. The Licensor warrants that it has, to the best of its knowledge, the rights to license reuse of the Licensed Material. However, you should ensure that the material you are requesting is original to the Licensor and does not carry the copyright of another entity (as credited in the published version).

1. 3. If the credit line on any part of the material you have requested indicates that it was reprinted or adapted with permission from another source, then you should also seek permission from that source to reuse the material.

2. Scope of Licence

2. 1. You may only use the Licensed Content in the manner and to the extent permitted by these Ts&Cs and any applicable laws.

2. 2. A separate licence may be required for any additional use of the Licensed Material, e.g. where a licence has been purchased for print only use, separate permission must be obtained for electronic re-use. Similarly, a licence is only valid in the language selected and does not apply for editions in other languages unless additional translation rights have been granted separately in the licence. Any content owned by third parties are expressly excluded from the licence.

2. 3. Similarly, rights for additional components such as custom editions and derivatives require additional permission and may be subject to an additional fee. Please apply to Journalpermissions@springernature.com/bookpermissions@springernature.com for these rights.

2. 4. Where permission has been granted **free of charge** for material in print, permission may also be granted for any electronic version of that work, provided that the material is incidental to your work as a whole and that the electronic version is essentially equivalent to, or substitutes for, the print version.

2. 5. An alternative scope of licence may apply to signatories of the STM Permissions Guidelines, as amended from time to time.

3. Duration of Licence

3. 1. A licence for is valid from the date of purchase ('Licence Date') at the end of the relevant period in the below table:

Scope of Licence	Duration of Licence
Post on a website	12 months
Presentations	12 months
Books and journals	Lifetime of the edition in the language purchased

4. Acknowledgement

4. 1. The Licensor's permission must be acknowledged next to the Licenced Material in print. In electronic form, this acknowledgement must be visible at the same time as the figures/tables/illustrations or abstract, and must be hyperlinked to the journal/book's homepage. Our required acknowledgement format is in the Appendix below.

5. Restrictions on use

5. 1. Use of the Licensed Material may be permitted for incidental promotional use and minor editing privileges e.g. minor adaptations of single figures, changes of format, colour and/or style where the adaptation is credited as set out in Appendix 1 below. Any other changes including but not limited to, cropping, adapting, omitting material that affect the meaning, intention or moral rights of the author are strictly prohibited.

5. 2. You must not use any Licensed Material as part of any design or trademark.

5. 3. Licensed Material may be used in Open Access Publications (OAP) before publication by Springer Nature, but any Licensed Material must be removed from OAP sites prior to final publication.

6. Ownership of Rights

6. 1. Licensed Material remains the property of either Licensor or the relevant third party and any rights not explicitly granted herein are expressly reserved.

7. Warranty

IN NO EVENT SHALL LICENSOR BE LIABLE TO YOU OR ANY OTHER PARTY OR ANY OTHER PERSON OR FOR ANY SPECIAL, CONSEQUENTIAL, INCIDENTAL OR INDIRECT DAMAGES, HOWEVER CAUSED, ARISING OUT OF OR IN CONNECTION WITH THE DOWNLOADING, VIEWING OR USE OF THE MATERIALS REGARDLESS OF THE FORM OF ACTION, WHETHER FOR BREACH OF CONTRACT, BREACH OF WARRANTY, TORT, NEGLIGENCE, INFRINGEMENT OR OTHERWISE (INCLUDING, WITHOUT LIMITATION, DAMAGES BASED ON LOSS OF PROFITS, DATA, FILES, USE, BUSINESS OPPORTUNITY OR CLAIMS OF THIRD PARTIES), AND
WHETHER OR NOT THE PARTY HAS BEEN ADVISED OF THE POSSIBILITY OF SUCH DAMAGES. THIS LIMITATION SHALL APPLY NOTWITHSTANDING ANY FAILURE OF ESSENTIAL PURPOSE OF ANY LIMITED REMEDY PROVIDED HEREIN.

8. Limitations

8. 1. ***BOOKS ONLY:***Where **'reuse in a dissertation/thesis'** has been selected the following terms apply: Print rights of the final author's accepted manuscript (for clarity,

NOT the published version) for up to 100 copies, electronic rights for use only on a personal website or institutional repository as defined by the Sherpa guideline (www.sherpa.ac.uk/romeo/).

8. 2. For content reuse requests that qualify for permission under the STM Permissions Guidelines, which may be updated from time to time, the STM Permissions Guidelines supersede the terms and conditions contained in this licence.

9. Termination and Cancellation

9. 1. Licences will expire after the period shown in Clause 3 (above).

9. 2. Licensee reserves the right to terminate the Licence in the event that payment is not received in full or if there has been a breach of this agreement by you.

Appendix 1 — Acknowledgements:

For Journal Content:
Reprinted by permission from [**the Licensor**]: [**Journal Publisher** (e.g. Nature/Springer/Palgrave)] [**JOURNAL NAME**] [**REFERENCE CITATION** (Article name, Author(s) Name), [**COPYRIGHT**] (year of publication)

For **Advance Online Publication papers:**
Reprinted by permission from [**the Licensor**]: [**Journal Publisher** (e.g. Nature/Springer/Palgrave)] [**JOURNAL NAME**] [**REFERENCE CITATION** (Article name, Author(s) Name), [**COPYRIGHT**] (year of publication), advance online publication, day month year (doi: 10.1038/sj.[JOURNAL ACRONYM].)

For Adaptations/Translations:
Adapted/Translated by permission from [**the Licensor**]: [**Journal Publisher** (e.g. Nature/Springer/Palgrave)] [**JOURNAL NAME**] [**REFERENCE CITATION** (Article name, Author(s) Name), [**COPYRIGHT**] (year of publication)

Note: For any republication from the British Journal of Cancer, the following credit line style applies:

Reprinted/adapted/translated by permission from [**the Licensor**]: on behalf of Cancer Research UK: : [**Journal Publisher** (e.g. Nature/Springer/Palgrave)] [**JOURNAL NAME**] [**REFERENCE CITATION** (Article name, Author(s) Name), [**COPYRIGHT]** (year of publication)

For **Advance Online Publication** papers:
Reprinted by permission from The [**the Licensor**]: on behalf of Cancer Research UK: [**Journal Publisher** (e.g. Nature/Springer/Palgrave)] [**JOURNAL NAME**] [**REFERENCE CITATION** (Article name, Author(s) Name), [**COPYRIGHT**] (year of publication), advance online publication, day month year (doi: 10.1038/sj.[JOURNAL ACRONYM])

For Book content:
Reprinted/adapted by permission from [**the Licensor**]: [**Book Publisher** (e.g.

Palgrave Macmillan, Springer etc) [**Book Title**] by [**Book author**(s)] [**COPYRIGHT**] (year of publication)

Other Conditions:

Version 1.3

Questions? customercare@copyright.com or +1-855-239-3415 (toll free in the US) or +1-978-646-2777.

Bibliography

[1] K. S Novoselov, A. K. Geim, S. V. Morozov, D. Jiang, Y. Zhang, S. V. Dubonos, I.V. Grigorieva, and A. A. Firsov. Electric Field Effect in Atomically Thin Carbon Films. *Science*, 306:666–669, 2004.

[2] Y. Yoon, K. Ganapathi, and S. Salahuddin. How Good Can Monolayer MoS_2 Transistors be? *Nano Lett.*, 11:3768–3773, 2011.

[3] K. F. Mak, C. Lee, J. Hone, J. Shan, and T. F. Heinz. Atomically Thin MoS_2: A New Direct-Gap Semiconductor. *Phys. Rev. Lett.*, 105:136805, 2010.

[4] F. K. Perkins, A. L. Friedman, E. Cobas, P. M. Campbell, G. G. Jernigan, and B. T. Jonker. Chemical Vapor Sensing with Monolayer MoS_2. *Nano Lett.*, 13:668–673, 2013.

[5] D. Sarkar, W. Liu, X. Xie, A. C. Anselmo, S. Mitragotri, and K. Banerjee. MoS_2 Field-Effect Transistor for Next-Generation Label-Free Biosensors. *ACS Nano*, 8:3992–4003, 2014.

[6] M. L. Tsai, S. H. Su, J. K. Chang, D. S. Tsai, C. H. Chen, C. I. Wu, L. J. Li, L. J. Chen, and J. H. He. Monolayer MoS_2 Heterojunction Solar Cells. *ACS Nano*, 8:8317–8322, 2014.

[7] A. K. Geim and I. V. Grigorieva. Van der Waals Heterostructures. *Nature*, 499:419–425, 2013.

[8] D. Jena, K. Banerjee, and G. H. Xing. 2D Crystal Semiconductors: Intimate Contacts. *Nat. Mater.*, 13:1076–1078, 2014.

[9] A. Allain, J. Kang, K. Banerjee, and A. Kis. Electrical Contacts to Two-Dimensional Semiconductors. *Nat. Mater.*, 14:1195–1205, 2015.

[10] I. Popov, G. Seifert, and D. Tománek. Designing Electrical Contacts to MoS_2 Monolayers: A Computational Study. *Phys. Rev. Lett.*, 108:156802, 2012.

[11] J. Kang, W. Liu, D. Sarkar, D. Jena, and K. Banerjee. Computational Study of Metal Contacts to Monolayer Transition-Metal Dichalcogenide Semiconductors. *Phys. Rev. X*, 4:031005, 2014.

[12] P. Zhang, Y. Zhang, Y. Wei, H. Jiang, X. Wang, and Y. Gong. Contact Engineering for Two-Dimensional Semiconductors. *J. Semicond.*, 39:071901, 2020.

[13] S. Das, Hong Y. Chen, A. V. Penumatcha, and J. Appenzeller. High Performance Multilayer MoS_2 Transistors With Scandium Contacts. *Nano Lett.*, 13:100–105, 2013.

[14] H. Yuan, G. Cheng, L. You, H. Li, H. Zhu, W. Li, J. J. Kopanski, Y. S. Obeng, A. R. Hight Walker, D. J. Gundlach, C. A. Richter, D. E. Ioannou, and Q. Li. Influence of Metal-MoS_2 Interface on MoS_2 Transistor Performance: Comparison of Ag and Ti Contacts. *ACS Appl. Mater. Inter.*, 7:1180–1187, 2015.

[15] J. Kang, W. Liu, and K. Banerjee. High-Performance MoS_2 Transistors With Low-Resistance Molybdenum Contacts. *Appl. Phys. Lett.*, 104:093106, 2014.

[16] W. Liu, D. Sarkar, J. Kang, W. Cao, and K. Banerjee. Impact of Contact on the Operation and Performance of Back-Gated Monolayer MoS_2 Field-Effect-Transistors. *ACS Nano*, 9:7904–7912, 2015.

[17] C. Gong, L. Colombo, R. M. Wallace, and K. Cho. The Unusual Mechanism of Partial Fermi Level Pinning at Metal-MoS_2 Interfaces. *Nano Lett.*, 14:1714–1720, 2014.

[18] M. Farmanbar and G. Brocks. Controlling the Schottky Barrier at MoS_2/Metal Contacts by Inserting a BN Monolayer. *Phys. Rev. B*, 91:161304, 2015.

[19] X. Cui, E. M. Shih, L. A. Jauregui, S. H. Chae, Y. D. Kim, B. Li, D. Seo, K. Pistunova, J. Yin, J. H. Park, H. J. Choi, Y. H. Lee, K. Watanabe, T. Taniguchi, P. Kim, C. R. Dean, and J. C. Hone. Low-Temperature Ohmic Contact to Monolayer MoS_2 by van der Waals Bonded Co/h-BN Electrodes. *Nano Lett.*, 17:4781–4786, 2017.

[20] J. L. Dye. Electrides: Early Examples of Quantum Confinement. *Acc. Chem. Res.*, 42:1564–1572, 2009.

[21] S. B. Dawes, D. L. Ward, R. H. Huang, and J. L. Dye. First Electride Crystal Structure. *J. Am. Chem. Soc.*, 108:3534–3535, 1986.

[22] D. L. Ward, R. H. Huang, and J. L. Dye. Structures of Alkalides and Electrides. I. Structure of Potassium Cryptand [2.2.2] Electride. *Acta Crystallogr. C*, 44:1374–1376, 1988.

[23] M. J. Wagner, R. H. Huang, J. L. Eglin, and J. L. Dye. An Electride With a Large Six-Electron Ring. *Nature*, 368:726–729, 1994.

[24] R. H. Huang, M. J. Wagner, D. J. Gilbert, K. A. Reidy-Cedergren, D. L. Ward, M. K. Faber, and J. L. Dye. Structure and Properties of Li^+(cryptand [2.1.1])e^-, an Electride With a 1D Spin-Ladder-Like Cavity-Channel Geometry. *J Am. Chem. Soc.*, 119:3765–3773, 1997.

[25] Q. Xie, R. H. Huang, A. S. Ichimura, R. C. Phillips, W. P. Pratt, and J. L. Dye. Structure and Properties of a New Electride, Rb^+(cryptand[2.2.2])e^-. *J. Am. Chem. Soc.*, 122:6971–6978, 2000.

[26] M. Y. Redko, J. E. Jackson, . H. Huang, and J. L. Dye. Design and Synthesis of a Thermally Stable Organic Electride. *J. Am. Chem. Soc.*, 127:12416–12422, 2005.

[27] S. Matsuishi, Y. Toda, M. Miyakawa, K. Hayashi, T. Kamiya, M. Hirano, I. Tanaka, and H. Hosono. High-Density Electron Anions in a Nanoporous Single Crystal: $[Ca_{24}Al_{28}O_{64}]^{4+}$ ($4e^-$). *Science*, 301:626–629, 2003.

[28] Y. Zhang, Z. Xiao, T. Kamiya, and H. Hosono. Electron Confinement in Channel Spaces for One-Dimensional Electride. *J. Phys. Chem. Letters*, 6:4966–4971, 2015.

[29] X. Zhang, Z. Xiao, H. Lei, Y. Toda, S. Matsuishi, T. Kamiya, S. Ueda, and H. Hosono. Two-Dimensional Transition-Metal Electride Y_2C. *Chem. Mater.*, 26:6638–6643, 2014.

[30] K. Lee, S. W. Kim, Y. Toda, S. Matsuishi, and H. Hosono. Dicalcium Nitride as a Two-Dimensional Electride With an Anionic Electron Layer. *Nature*, 494:336–340, 2013.

[31] D. H. Gregory, A. Bowman, C. F. Baker, and D. P. Weston. Dicalcium Nitride, Ca_2N - A 2D 'Excess Electron' Compound; Synthetic Rotates and Crystal Chemistry. *J. Mater. Chem.*, 10:1635–1641, 2000.

[32] E. T. Keve and A. C. Skapski. The Crystal Structure of Dicalcium Nitride. *Inorg. Chem.*, 7:1757–1761, 1968.

[33] C. M. Fang, G. A. De Wijs, R. A. De Groot, H. T. Hintzen, and G. De With. Bulk and Surface Electronic Structure of the Layered Sub-Nitrides Ca_2N and Sr_2N. *Chem. Mater.*, 12:1847–1852, 2000.

[34] J. S. Oh, C. J. Kang, Y. J. Kim, S. Sinn, M. Han, Y. J. Chang, B. G. Park, S. W. Kim, B. I. Min, H. Do Kim, and T. W. Noh. Evidence for Anionic Excess Electrons in a Quasi-Two-Dimensional Ca_2N Electride by Angle-Resolved Photoemission Spectroscopy. *J. Am. Chem. Soc.*, 138:2496–2499, 2016.

[35] T. Tada, S. Takemoto, S. Matsuishi, and H. Hosono. High-Throughput ab Initio Screening for Two-Dimensional Electride Materials. *Inorg. Chem.*, 53:10347–10358, 2014.

[36] T. Inoshita, S. Jeong, N. Hamada, and H. Hosono. Exploration for Two-Dimensional Electrides via Database Screening and ab Initio Calculation. *Phys. Rev. X*, 4:031023, 2014.

[37] W. Ming, M. Yoon, M. H. Du, K. Lee, and S. W. Kim. First-Principles Prediction of Thermodynamically Stable Two-Dimensional Electrides. *J. Am. Chem. Soc.*, 138:15336–15344, 2016.

[38] Y. Zhang, H. Wang, Y. Wang, L. Zhang, and Y. Ma. Computer-Assisted Inverse Design of Inorganic Electrides. *Phys. Rev. X*, 7:011017, 2017.

[39] C. Park, S. W. Kim, and M. Yoon. First-Principles Prediction of New Electrides with Nontrivial Band Topology Based on One-Dimensional Building Blocks. *Phys. Rev. Lett.*, 120:026401, 2018.

[40] S. Kim, S. Song, J. Park, H. S. Yu, S. Cho, D. Kim, J. Baik, D. H. Choe, K. J. Chang, Y. H. Lee, S. W. Kim, and H. Yang. Long-Range Lattice Engineering of $MoTe_2$ by a 2D Electride. *Nano Lett.*, 17:3363–3368, 2017.

[41] M. M. Menamparambath, J. H. Park, H. S. Yoo, S. P. Patole, J. B. Yoo, S. W. Kim, and S. Baik. Large Work Function Difference Driven Electron Transfer From Electrides to Single-Walled Carbon Nanotubes. *Nanoscale*, 6:8844–8851, 2014.

[42] M. Kitano, Y. Inoue, H. Ishikawa, K. Yamagata, T. Nakao, T. Tada, S. Matsuishi, T. Yokoyama, M. Hara, and H. Hosono. Essential Role of Hydride Ion in Ruthenium-Based Ammonia Synthesis Catalysts. *Chem. Sci.*, 7:4036–4043, 2016.

[43] Y. Kobayashi, M. Kitano, S. Kawamura, T. Yokoyama, and H. Hosono. Kinetic Evidence: The Rate-Determining Step for Ammonia Synthesis Over Electride-Supported Ru Catalysts is no Longer the Nitrogen Dissociation Step. *Catal. Sci. Technol.*, 7:47–50, 2017.

[44] J. Hu, B. Xu, S. A. Yang, S. Guan, C. Ouyang, and Y. Yao. 2D Electrides as Promising Anode Materials for Na-Ion Batteries From First-Principles Study. *ACS Appl. Mater. Inter.*, 7:24016–24022, 2015.

[45] S. Zhao, Z. Li, and J. Yang. Obtaining Two-Dimensional Electron Gas in Free Space Without Resorting to Electron Doping: An Electride Based Design. *J. Am. Chem. Soc.*, 136:13313–13318, 2014.

[46] S. Guan, S. A. Yang, L. Zhu, J. Hu, and Y. Yao. Electronic, Dielectric, and Plasmonic Properties of Two-Dimensional Electride Materials X_2N (X=Ca, Sr): A First-Principles Study. *Sci. Rep-UK*, 5:12285, 2015.

[47] D. L. Druffel, K. L. Kuntz, A. H. Woomer, F. M. Alcorn, J. Hu, C. L. Donley, and S. C. Warren. Experimental Demonstration of an Electride as a 2D Material. *J. Am. Chem. Soc.*, 138:16089–16094, 2016.

[48] S. G. Dale and E. R. Johnson. The Ionic: Versus Metallic Nature of 2D Electrides: A Density-Functional Description. *Phys. Chem. Chem. Phys.*, 19:27343–27352, 2017.

[49] X. Zeng, S. Zhao, Z. Li, and J. Yang. Electron-Phonon Interaction in a Ca_2N Monolayer: Intrinsic Mobility of Electrene. *Phys. Rev. B*, 98:155443, 2018.

[50] G. Abbas, S. Zhao, Z. Li, and J. Yang. Obtaining Intrinsically Occupied Free-Space Superatom States in an Encapsulated Ca_2N Nanotube. *ACS Omega*, 3:11966–11971, 2018.

[51] Q. Tang. Enhanced 1T'-Phase Stabilization and Chemical Reactivity in a $MoTe_2$ Monolayer through Contact with a 2D Ca_2N Electride. *ChemPhysChem*, 20:595–601, 2019.

[52] K. P. Dhakal, G. Ghimire, K. Chung, D. L. Duong, S. W. Kim, and J. Kim. Probing Multiphased Transition in Bulk MoS2 by Direct Electron Injection. *ACS Nano*, 13:14437–14446, 2019.

[53] P. Giannozzi, S. Baroni, N. Bonini, M. Calandra, R. Car, C. Cavazzoni, D. Ceresoli, G. L. Chiarotti, M. Cococcioni, I. Dabo, A. Dal Corso, S. De Gironcoli, S. Fabris, G. Fratesi, R. Gebauer, U. Gerstmann, C. Gougoussis, A. Kokalj, M. Lazzeri, L. Martin-Samos, N. Marzari, F. Mauri, R. Mazzarello, S. Paolini, A. Pasquarello, L. Paulatto, C. Sbraccia, S. Scandolo, G. Sclauzero, A. P. Seitsonen, A. Smogunov, P. Umari, and R. M. Wentzcovitch. QUANTUM ESPRESSO: A Modular and Open-Source Software Project for Quantum Simulations of Materials. *J. Phys. Condens. Matter*, 21:395502, 2009.

[54] F. Bloch. Über die Quantenmechanik der Elektronen in Kristallgittern. *Z. Phys.*, 52:555–600, 1929.

[55] L. Brillouin. Les Électrons Libres Dans les Métaux et le Role des Réflexions de Bragg. *J. Phys. Radium*, 1:377–400, 1930.

[56] P. Hohenberg and W. Kohn. Inhomogeneous Electron Gas. *Phys. Rev.*, 136:864–871, 1964.

[57] W. Kohn and L. J. Sham. Self-Consistent Equations Including Exchange and Correlation Effects. *Phys. Rev.*, 140:1133–1138, 1965.

[58] A. D. Becke. Density-Functional Exchange-Energy Approximation with Correct Asymptotic Behavior. *Phys. Rev. A*, 38:3098–3100, 1988.

[59] J. P. Perdew, K. Burke, and M. Ernzerhof. Generalized Gradient Approximation Made Simple. *Phys. Rev. Lett.*, 77:3865–3868, 1996.

[60] A. D. Becke and E. R. Johnson. Exchange-Hole Dipole Moment and the Dispersion Interaction Revisited. *J. Chem. Phys.*, 127:154108, 2007.

[61] E. R. Johnson. The Exchange-Hole Dipole Moment Dispersion Model. In A Otero-de-la-Roza and G A DiLabio, editors, *Non-Covalent Interactions in Quantum Chemistry and Physics*, chapter 5, pages 169–194. Elsevier, 2017.

[62] A. Otero-de-la-Roza and E. R. Johnson. Van der Waals Interactions in Solids Using the Exchange-Hole Dipole Moment. *J. Chem. Phys.*, 136:174109, 2012.

[63] A. Otero-de-la-Roza, L. M. LeBlanc, and E. R. Johnson. Asymptotic Pairwise Dispersion Corrections Can Describe Layered Materials Accurately. *J. Phys. Chem. Lett.*, 11:2298–2302, 2020.

[64] P. Schwerdtfeger. The Pseudopotential Approximation in Electronic Structure Theory. *ChemPhysChem*, 12:3143–3155, 2011.

[65] P. E. Blöchl. Projector Augmented-Wave Method. *Phys. Rev. B*, 50:17953–17979, 1994.

[66] G. Kresse and D. Joubert. From Ultrasoft Pseudopotentials to the Projector Augmented-Wave Method. *Phys. Rev. B*, 59:1758–1775, 1999.

[67] J. W. Zwanziger. Computation of NMR Observables: Consequences of Projector-Augmented Wave Sphere Overlap. *Solid State Nucl. Magn. Reson.*, 80:14–18, 2016.

[68] A. Dal Corso. Pseudopotentials Periodic Table: From H to Pu. *Comput. Mater. Sci.*, 95:337–350, 2014.

[69] H. J. Monkhorst and J. D. Pack. Special Points for Brillouin-Zone Integrations. *Phys. Rev. B*, 13:5188–5192, 1976.

[70] D. Sanchez-Portal, E. Artacho, and J. M. Soler. Projection of Plane-Wave Calculations Into Atomic Orbitals. *Solid State Commun.*, 95:685–690, 1995.

[71] R. F. W. Bader. *Atoms in Molecules: A Quantum Theory.* Oxford University Press, Oxford, 1990.

[72] R. S. Mulliken. Electronic Population Analysis on LCAO. *J. Chem. Phys*, 23:1833, 1955.

[73] F. L. Hirshfeld. Bonded-Atom Fragments for Describing Molecular Charge Densities. *Theor. Chim. Acta*, 44:129–138, 1977.

[74] M. Yu and D. R. Trinkle. Accurate and Efficient Algorithm for Bader Charge Integration. *J. Chem. Phys.*, 134:064111, 2011.

[75] T. Inoshita, S. Takemoto, T. Tada, and H. Hosono. Surface Electron States on the Quasi-Two-Dimensional Excess-Electron Compounds Ca_2N and Y_2C. *Phys. Rev. B*, 95:165430, 2017.

[76] J. Wang, L. Li, Z. Shen, P. Guo, M. Li, B. Zhao, L. Fang, and L. Yang. Ultralow Interlayer Friction of Layered Electride Ca_2N: A Potential Two-Dimensional Solid Lubricant Material. *Materials*, 11, 2018.

[77] A. J. A. Price, K. R. Bryenton, and E. R. Johnson. Requirements for an accurate dispersion-corrected density functional. *J. Chem. Phys.*, 154:230902, 2021.

[78] R.W.G Wyckoff. *Crystal Structures*. Interscience Publishers, New York, 1963.

[79] C. F. Baker, M. G. Barker, and A. J. Blake. Calcium Nitride (Ca_2N), a Redetermination. *ACTA Crystallogr. E*, 57:i6–i7, 2001.

[80] R. F. W. Bader. A Quantum-Theory of Molecular-Structure and its Applications. *Chem. Rev.*, 91:893–928, 1991.

[81] A. Otero-de-la-Roza, E. R Johnson, and V. Luaña. Critic2: A Program for Real-Space Analysis of Quantum Chemical Interactions in Solids. *Comput. Phys. Commun.*, 185:1007–1018, 2014.

[82] H. Tang, B. Wan, B. Gao, Y. Muraba, Q. Qin, B. Yan, P. Chen, Q. Hu, D. Zhang, L. Wu, M. Wang, H. Xiao, H. Gou, F. Gao, H. Ho-kwang Mao, and H. Hosono. Metal-to-Semiconductor Transition and Electronic Dimensionality Reduction of Ca_2N Electride Under Pressure. *Adv. Sci.*, 5:1800666, 2018.

[83] X. L. Qiu, J. F. Zhang, Z. Y. Lu, and K. Liu. Manipulating the Electronic and Magnetic Properties of Monolayer Electride Ca_2N by Hydrogenation. *J. Phys. Chem. C*, 123:24698–24704, 2019.

[84] D. L. Druffel, A. H. Woomer, K. L. Kuntz, J. T. Pawlik, and S. C. Warren. Electrons on the Surface of 2D Materials: From Layered Electrides to 2D Electrenes. *J. Mater. Chem. C*, 5:11196–11213, 2017.